



**SUSTAINABLE ACTIVATED CARBON FROM HEMP
BIOWASTE: DUAL HETEROATOM DOPING FOR
ENHANCED SUPERCAPACITOR PERFORMANCE**

BY

PATTARAMON MEEFANG

**A THESIS SUBMITTED IN PARTIAL FULFILLMENT OF
THE REQUIREMENTS FOR THE DEGREE OF
MASTER OF SCIENCE (CHEMISTRY)
DEPARTMENT OF CHEMISTRY
FACULTY OF SCIENCE AND TECHNOLOGY
THAMMASAT UNIVERSITY
ACADEMIC YEAR 2024**

**SUSTAINABLE ACTIVATED CARBON FROM HEMP
BIOWASTE: DUAL HETEROATOM DOPING FOR
ENHANCED SUPERCAPACITOR PERFORMANCE**

BY

PATTARAMON MEEFANG

**A THESIS SUBMITTED IN PARTIAL FULFILLMENT OF
THE REQUIREMENTS FOR THE DEGREE OF
MASTER OF SCIENCE (CHEMISTRY)
DEPARTMENT OF CHEMISTRY
FACULTY OF SCIENCE AND TECHNOLOGY
THAMMASAT UNIVERSITY
ACADEMIC YEAR 2024**

THAMMASAT UNIVERSITY
FACULTY OF SCIENCE AND TECHNOLOGY

THESIS

BY

PATTARAMON MEEFANG

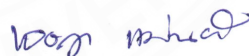
ENTITLED

SUSTAINABLE ACTIVATED CARBON FROM HEMP BIOWASTE: DUAL
HETEROATOM DOPING FOR ENHANCED SUPERCAPACITOR
PERFORMANCE

was approved as partial fulfillment of the requirements for
the degree of Master of Science (Chemistry)

on December 20, 2024

Chairman



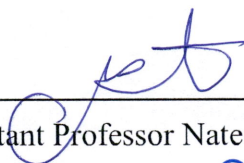
(Jedsada Manyam, Ph.D.)

Member and Advisor



(Associate Professor Peerasak Paoprasert, Ph.D.)

Member



(Assistant Professor Natee Sirisit, Ph.D.)

Dean



(Associate Professor Supet Jirakajohnkool, Ph.D.)

Thesis Title	Sustainable Activated Carbon from Hemp Biowaste: Dual Heteroatom Doping for Enhanced Supercapacitor Performance
Author	Pattaramon Meefang
Degree	Master of Science (Chemistry)
Department/Faculty/University	Department of Chemistry Faculty of Science and Technology Thammasat University
Thesis Advisor	Associate Professor Peerasak Paoprasert, Ph.D.
Academic Year	2024

ABSTRACT

Energy consumption is growing exponentially these days, prompting the need for the development of energy storage systems. In this work, the synthesis of N, S-dual-doped activated carbon from hemp cores was developed for high-performance supercapacitors. Conversion of hemp core biomass into N, S-dual-doped activated carbon using thiourea as nitrogen and sulfur sources via activation process was generated.

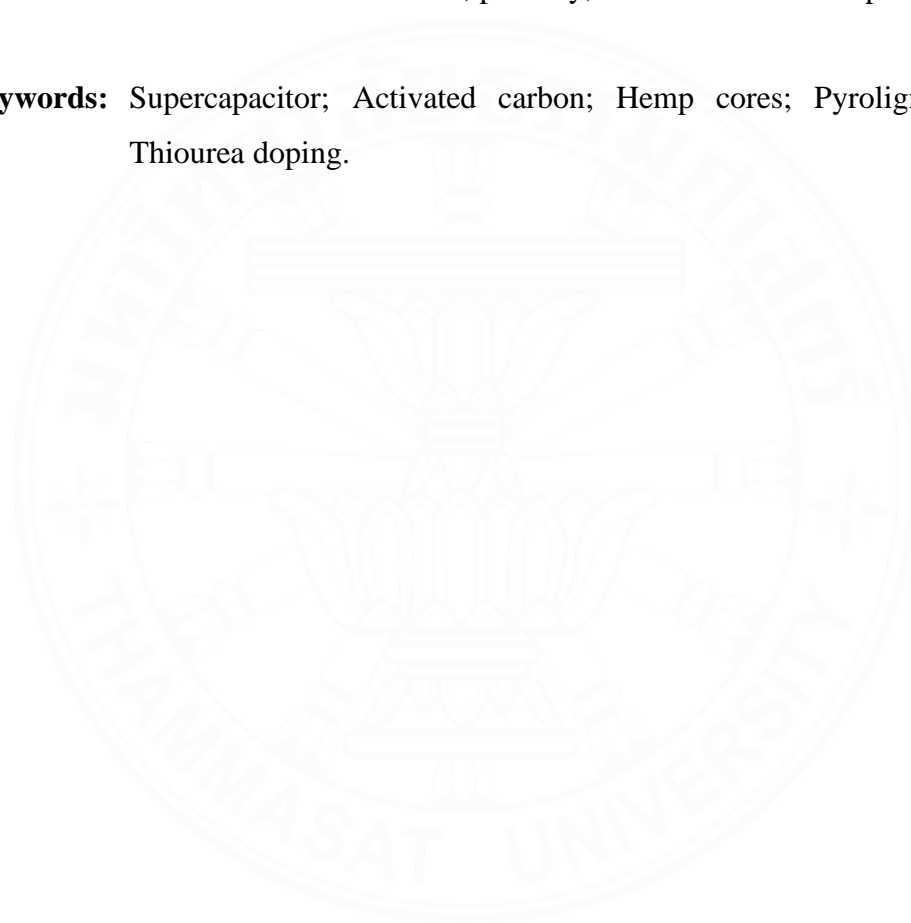
The research focuses on the synthesis factors of activated carbon by comparing thiourea doping levels of 10%wt and 20%wt, as well as activation temperatures. Results indicate that supercapacitor performance is influenced by several factors, including surface area and N and S content. Specifically, at 800°C, thiourea doping increased the specific surface area by 1.2 times, while extreme conditions led to a lack of N and S, resulting in poor performance (175 F g⁻¹). Conversely, at 700°C, thiourea doping improved the specific surface area by 1.46 times and incorporated N and S into the structure, yielding a specific capacitance of 510 F g⁻¹ for the 10%wt thiourea-doped carbon (AC700-2).

Utilizing pyroligneous acid from hemp charcoal production as an electrolyte further enhanced performance, achieving a specific capacitance of 672 F g⁻¹—1.32 times higher than the control electrolyte. The highest energy density

recorded was 106 Wh kg^{-1} at a power density of 999.9 W kg^{-1} in a supercapacitor using N, S activated carbon in a 3M KOH/PA electrolyte.

The evaluation of the electrochemical performance indicates that activated carbon and electrolyte generated from hemp cores could potentially be used as a promising electrode material and electrolyte in an electrochemical energy storage supercapacitor. This study indicates that the doping of nitrogen and sulfur into activated carbon exhibited enhanced surface area, porosity, and electrochemical performance.

Keywords: Supercapacitor; Activated carbon; Hemp cores; Pyroligneous acid; Thiourea doping.



ACKNOWLEDGEMENTS

I would like to express my deepest appreciation to all those who have supported and guided me throughout my thesis journey.

First and foremost, I extend my heartfelt gratitude to Associate Professor Peerasak Paoprasert, my advisor, whose invaluable guidance, encouragement, and insights have played a pivotal role in shaping this research.

I am also deeply thankful to the Department of Chemistry at Thammasat University for providing the necessary resources and opportunities that made this research possible.

To my colleagues and lab members, your collaboration, encouragement, and thought-provoking discussions have been immensely supportive throughout this process, and I am truly grateful for your contributions.

Lastly, I am profoundly thankful to my family and friends for their unwavering love, patience, and encouragement. Your belief in me has been a constant source of strength during the most challenging moments of this journey.

Pattaramon Meefang

TABLE OF CONTENTS

	Page
ABSTRACT	(1)
ACKNOWLEDGEMENTS	(3)
LIST OF TABLES	(7)
LIST OF FIGURES	(8)
LIST OF ABBREVIATIONS	(11)
CHAPTER 1 INTRODUCTION	1
1.1 Problem statement	1
1.2 Background of biomass material	2
1.3 Research objectives	3
1.4 Scope and limitation of the study	3
CHAPTER 2 REVIEW OF LITERATURE	5
2.1 Background of energy storage	5
2.2 Supercapacitor	6
2.2.1 Electrode material	7
2.2.2 Electrolyte	7
2.3 Activated carbon (AC)	8
2.4 Modification of AC	12
2.4.1 Nitrogen doped AC	12
2.4.2 Nitrogen, Sulfur co-doped AC	14
2.5 Raw material	14

	(7)
2.5.1 Hemp	14
2.5.2 Pyroligneous acid (PA)	18
CHAPTER 3 RESEARCH METHODOLOGY	25
3.1 Materials and chemicals	25
3.2 Synthesis of electrode materials	25
3.2.1 Hemp-derived activated carbon (HAC)	25
3.2.2 Hemp-derived N,S co-doped activated carbon (N,S-HAC)	25
3.3 Fabrication of electrodes	26
3.4 Electrolyte preparation	27
3.5 Characterization	27
3.6 Electrochemical measurements	27
3.7 Calculations	28
CHAPTER 4 RESULTS AND DISCUSSION	29
4.1 Synthesis and characterization of AC800	29
4.2 Synthesis and characterization of AC700	34
4.3 Electrochemical performance of AC800	40
4.4 Electrochemical performance of AC700	41
4.5 Electrochemical properties of Pyroligneous acid electrolytes	43
4.6 Analysis of capacitance contribution	46
4.7 Contact angle measurement	48
CHAPTER 5 CONCLUSIONS AND RECOMMENDATIONS	50
5.1 Conclusion	50
5.2 Recommendations	51
REFERENCES	52
APPENDICES	59

(8)

APPENDIX A CHARACTERIZATION 60

APPENDIX B ELECTROCHEMICAL MEASUREMENTS 61

BIOGRAPHY 64



LIST OF TABLES

Tables	Page
2.1 Previous research on Hemp-derived activated carbon	11
2.2 Advantages and drawbacks in the modification of AC	12
2.3 Chemical composition of hemp	17
2.4 Previous research on Hemp-derived activated carbon for EDLC applications	18
2.5 Properties of PA	21
2.6 Chemical composition of PA from GC-MS analysis	22
3.1 Different type of activated carbon	26
4.1 The characterization of AC800	34
4.2 The characterization of AC700	38
1B Specific capacitance of AC different type electrode in 3M KOH electrolyte	61
2B Specific capacitance of AC700 in 3M KOH electrolyte in different scan rate	61
3B Specific capacitance of AC700 in 3M KOH/PA electrolyte in different scan rate	62

LIST OF FIGURES

Figures	Page
2.1 Ragone plot for different storage devices	5
2.2 Schematic diagram of supercapacitors. (a) EDLC; (b) Pseudocapacitor	6
2.3 Types of electrolytes for supercapacitors	7
2.4 Schematic presentation of pore structure and surface functional groups of activated carbon	8
2.5 Schematic production process of activated carbon from biomass and char by physical or chemical activation	9
2.6 Schematic diagram of KOH activation process	11
2.7 Structure of N-doped AC	13
2.8 Structure and morphology of N, S-doped AC	14
2.9 Hemp	15
2.10 Products and uses of hemp	16
2.11 Chemical composition of plant	17
2.12 Color of pyroligneous acid	19
2.13 Production of pyroligneous acid	19
4.1 Schematic of hemp-based supercapacitor	29
4.2 (a) N ₂ adsorption-desorption isotherm, (b) pore-size distributions, (c) XRD patterns, and (d) Raman spectrum of AC800	31
4.3 (a,d) SEM image of AC800-1, (b,e) SEM image of AC800-2, and (c,f) SEM image of AC800-3	31
4.4 The survey XPS spectrum of AC800 (a) AC800-1, (b) AC800-2, and (c) AC800-3	32
4.5 (a) high-resolution spectra C _{1s} of AC800-1, (b) high-resolution spectra O _{1s} of AC800-1, (c) high-resolution spectra C _{1s} of AC800-2, (d) high-resolution spectra O _{1s} of AC800-2, (e) high-resolution spectra C _{1s} of AC800-3, and high-resolution spectra O _{1s} of AC800-3	33

4.6 (a) N ₂ adsorption-desorption isotherm and (b) pore-size distributions, (c) XRD patterns and Raman spectra of the AC700	35
4.7 (a,d) SEM image of AC700-1, (b,c) SEM image of AC700-2, and (c,f) SEM image of AC700-3	37
4.8 The survey XPS spectrum of AC700 (a) AC700-1, (b) AC700-2, and (c) AC700-3	38
4.9 (a) high-resolution spectra of C _{1s} , (b) high-resolution spectra of N _{1s} , (c) high-resolution spectra of O _{1s} , and (d) high-resolution spectra of S _{2p} , of AC700-2	39
4.10 (a) high-resolution spectra C _{1s} , (b) high-resolution spectra N _{1s} , (c) high-resolution spectra O _{1s} of AC800-2, (d) high-resolution spectra S _{2p} of AC700-3	40
4.11 (a) CV curves comparison of various electrode at scan rate 30 mV s ⁻¹ , (b) CV curves of AC700-1 electrode at different scan rates (5, 10, 30, 50, 70 and 100 mV s ⁻¹)	41
4.12 (a) CV curves of AC electrode in 3M KOH electrolyte at a scan rate of 30 mV s ⁻¹ , (b) GCD curves of AC electrode in 3M KOH electrolyte at current density of 2.5 A g ⁻¹ , (c) EIS spectra of AC electrode in 3M KOH electrolyte, and (d) capacitance retention of AC700-2 in 3M KOH electrolyte	42
4.13 Probable reversible redox reactions due to N, S doping	43
4.14 (a) CV curves of mixing various concentrations of KOH in PA, (b) CV curves of AC700-2 electrode in 3M KOH/PA electrolyte at different scan rates (5, 10, 30, 50, 70 and 100 mV s ⁻¹), (c) GCD curve of all types of AC in 3M KOH/PA, and (d) GCD curve of AC700-2 electrode in 3M KOH/PA electrolyte at different current densities (2,2.5,3, 3.5,4 and 4.5 A g ⁻¹)	44
4.15 (a) EIS spectra of AC electrode in 3M KOH/PA electrolyte, and (b) capacitance retention of AC700-2 in 3M KOH/PA electrolyte	45

4.16 (a) Ratio between surface contribution and diffusion contribution of AC700 electrode in 3M KOH electrolyte, (b) Ratio of AC700-1 at scan rate 30 mV s^{-1} , (c) Ratio of AC700-2 at scan rate 30 mV s^{-1} , and (d) Ratio of AC700-3 at scan rate 30 mV s^{-1}	47
4.17 (a) Ratio between surface contribution and diffusion contribution of AC700 electrode in 3M KOH/PA electrolyte, (b) Ratio of AC700-1 at scan rate 30 mV s^{-1} , (c) Ratio of AC700-2 at scan rate 30 mV s^{-1} , and (d) Ratio of AC700-3 at scan rate 30 mV s^{-1}	48
4.18 Contact angle of AC700 electrode in 3M KOH electrolyte compared to 3M KOH/PA electrolyte	49
1A (a) high-resolution spectra of C_{1s} , (b) high-resolution spectra of N_{1s} , (c) high-resolution spectra of O_{1s} , (d) Survey XPS spectra of AC700-1	60
1B Relative between specific capacitance and scan rate of AC700 electrode and 3M KOH electrolyte	62
2B Relative between specific capacitance and scan rate of AC700 electrode and 3M KOH/PA electrolyte	63
3B Equivalent circuit of supercapacitor	63

LIST OF ABBREVIATIONS

Symbols/Abbreviations	Terms
% wt	Weight percent
°C	Degree Celsius
A g ⁻¹	Ampere per gram
AC	Activated Carbon
Ag	Silver
AgCl	Silver chloride
BET	Brunauer-Emmett-Teller
BJH	Barret-Joner-Halenda
CB	Carbon black
cm ⁻¹	Per centimeter
cm ³ g ⁻¹	Cubic centimeter per gram
C _{sp}	Specific capacitance
CV	Cyclic Voltammetry
E	Energy density
EDLC	Electric double-layer capacitor
EIS	Electrochemical impedance spectroscopy
eV	Electron volt
F g ⁻¹	Farad per gram
g	Gram
GCD	Galvanostatic charge-discharge
h	Hour
HCl	Hydrochloric acid
H ₂ SO ₄	Sulfuric acid
KOH	Potassium hydroxide
M	Molar
m ² g ⁻¹	Square meter per gram
mg	Milligram

Symbols/Abbreviations	Terms
mL	Milliliter
mV	Millivolt
mV s ⁻¹	Millivolt per second
N ₂	Nitrogen gas
nm	Nanometer
NMP	N-Methyl-2-pyrrolidone
P	Power density
pH	Potential of hydrogen ion
Pt	Platinum
PVDF	Polyvinylidene fluoride
R _s	Equivalent series resistance
R _{ct}	Charge transfer resistance
SEM	Scanning electron microscope
V	Volt
Wh kg ⁻¹	Watt-hour per kilogram
XPS	X-ray photoelectron spectroscopy
μm	Micrometer
Ω	Ohm

CHAPTER 1

INTRODUCTION

1.1 Problem statement

Nowadays, the increasing emphasis on environmental sustainability has led to a rapid surge in the development and deployment of renewable energy sources. As a result, the importance of energy storage devices has escalated at a remarkable pace. The urgency to adopt renewable energy solutions stems from concerns about climate change, pollution, and the finite nature of fossil fuel resources. However, renewable energy, such as solar and wind power, can be intermittent due to weather conditions and other factors. Energy storage plays a pivotal role in mitigating this intermittent by storing surplus energy during periods of high generation and supplying it when demand is elevated, or generation is low.

Energy storage is a complex process that involves various forms and technologies. Battery energy storage (lithium-ion batteries, flow batteries, and lead-acid batteries), is widely used in portable electronics and electric vehicles due to their high energy density. Mechanical energy storage, such as pumping hydro storage and flywheel energy storage, involves pumping water uphill to a reservoir during excess energy and releasing it through turbines to generate electricity during peak demand. Supercapacitors store energy electrostatically and have high power density (Ibrahim, Ilinca, & Perron, 2008; Koochi-Fayegh & Rosen, 2020; Olabi, 2017).

In order to preserve the environment as much as possible, using biological waste for maximum benefit is an important choice because it conserves energy and the environment. Biological waste can indeed be transformed into various forms of carbon materials through different processes. Biomass, which includes organic materials such as agricultural residues, wood waste, food waste, and certain types of industrial waste, can be converted into carbon-based materials like biochar, activated carbon, or carbon nanomaterials.

Because of its high-power density, long cycle life, fast charging and discharging process, high efficiency compared to batteries, and wide operating

temperature range, supercapacitors have attracted the curiosity of researchers. Supercapacitors store energy through electrostatic storage, a mechanism different from traditional batteries. They consist of two electrodes with an electrolyte solution, and when a voltage is applied, an electric field is created, causing ions from the electrolyte to accumulate on the electrodes. The majority of energy storage occurs through double-layer capacitance (EDLC) and pseudocapacitance, which involves a reversible faradaic redox reaction at the electrode surface (Conway, Birss, & Wojtowicz, 1997; Libich, Máca, Vondrák, Čech, & Sedlářiková, 2018; Mclean, Virginia, Halper, & Ellenbogen, 2006; Shao et al., 2018; Shukla, Sampath, & Vijayamohanan, 2000; Vangari, Pryor, & Jiang, 2013; Zhao & Burke, 2021).

The insufficient energy density of supercapacitors can be compensated by using high specific capacitance materials as electrodes, such as highly porous activated carbon. Furthermore, this problem may be reduced by using proper electrolytes to produce a broad potential window. As a result, both high specific capacitance materials and high voltage window electrolytes help to enhance energy density.

1.2 Background of biomass material

Hemp (*Cannabis sativa* L. Subsp. *sativa*) is one of the oldest cultivated plants by humans. It is believed to have originated in Central Asia. Archaeological evidence suggests that hemp was used in China as early as 8000 BCE for its fibers to make textiles, ropes, and paper, and then cultivation spread throughout Asia, Europe, and the Middle East. It played a vital role in several ancient cultures, such as in ancient India for medicinal purposes, in ancient Egypt for making ropes and textiles, and in ancient Greece and Rome for various applications, including textiles and food. Nowadays, hemp is gaining recognition for its sustainability, environmental benefits, and diverse applications across various industries. Countries are revisiting their legislation to allow for controlled cultivation and use of hemp, recognizing its economic potential and the numerous products that can be derived from this versatile plant (Hartsel, Eades, Hickory, & Makriyannis, 2016).

Hemp core biomass waste refers to the fibrous inner part of the hemp plant stalk that remains after the extraction of hemp fibers, seeds, or other valuable

components. This hemp core, also known as hemp hurds or shives, is considered a byproduct of hemp processing.

In this work, the maximum utilization of bio-waste materials is presented to consider the environmental impact by using the useless waste components of hemp as major materials for the synthesis of electrode materials and pyroligneous acid from hemp char preparation is used as an electrolyte to achieve the most efficient use of biological waste.

1.3 Research objectives

- 1.3.1 To synthesize and characterize activated carbon from hemp cores.
- 1.3.2 To optimize the suitable amount of thiourea content in the precursor.
- 1.3.3 To fabricate electrodes from hemp core-derived activated carbon.
- 1.3.4 To enhance the electrochemical properties of prepared electrodes.
- 1.3.5 To fabricate high-performance symmetric supercapacitor using activated carbon from hemp cores as electrode and pyroligneous acid by product of synthetic carbon char as electrolyte.

1.4 Scope and limitation of the study

1.4.1 To synthesize activated carbon from hemp core as a raw material using the hydrothermal method and thermal activation.

1.4.2 To study the effects of the following activation parameters on the properties of activated carbon.

- 1.4.2.1 Ratio of the chemical dopant (thiourea) to activated carbon
- 1.4.2.2 Activation temperature
- 1.4.2.3 Heat rate of activation process
- 1.4.3 Characterization of prepared activated carbon
 - 1.4.3.1 Structure characterizations
 - X-ray diffraction (XRD)
 - Raman spectroscopy
 - 1.4.3.2 Size measurements

- Nitrogen adsorption-desorption

1.4.3.3 Element content

- X-ray photoelectron spectroscopy (XPS)

1.4.3.4 Morphological characterization

- Scanning electron microscope (SEM)
- Contact angle measurement

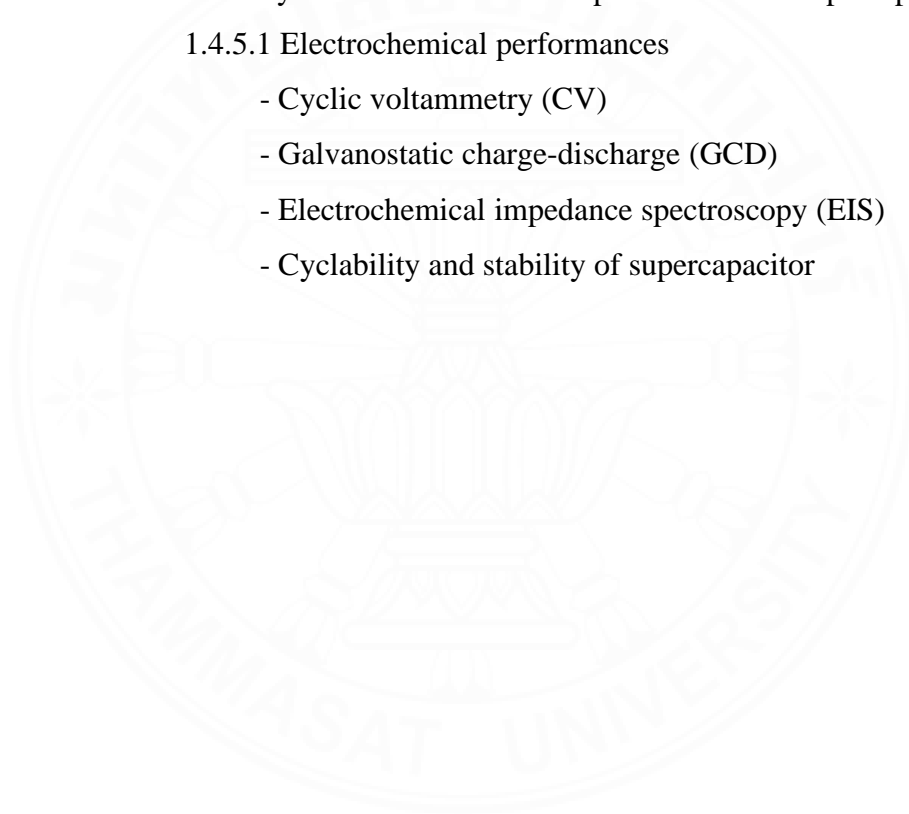
1.4.4 Preparation of pyroligneous acid electrolyte via following parameters

1.4.4.1 Ratio between base and pyroligneous acid

1.4.5 To study of the electrochemical performance of supercapacitor

1.4.5.1 Electrochemical performances

- Cyclic voltammetry (CV)
- Galvanostatic charge-discharge (GCD)
- Electrochemical impedance spectroscopy (EIS)
- Cyclability and stability of supercapacitor



CHAPTER 2

REVIEW OF LITERATURE

2.1 Background of energy storage

The design of batteries has certain limitations, particularly in their ability to deliver power rapidly. Rapid energy bursts, such as those required for load stabilization or powering motors, can strain the battery, reduce its capacity, and shorten its lifespan. This limitation arises from the low energy density or specific energy of batteries. Consequently, utilizing batteries for applications that demand rapid bursts of energy can be challenging.

In contrast, supercapacitors are specifically designed for rapid energy delivery. While batteries can store significantly more energy and retain it for longer periods due to their higher specific energy, supercapacitors can deliver energy up to 10 times faster than batteries (Ibrahim et al., 2008; Kazempour, Moghaddam, Haghifam, & Yousefi, 2009; J. Liu et al., 2018; Zhao & Burke, 2021).

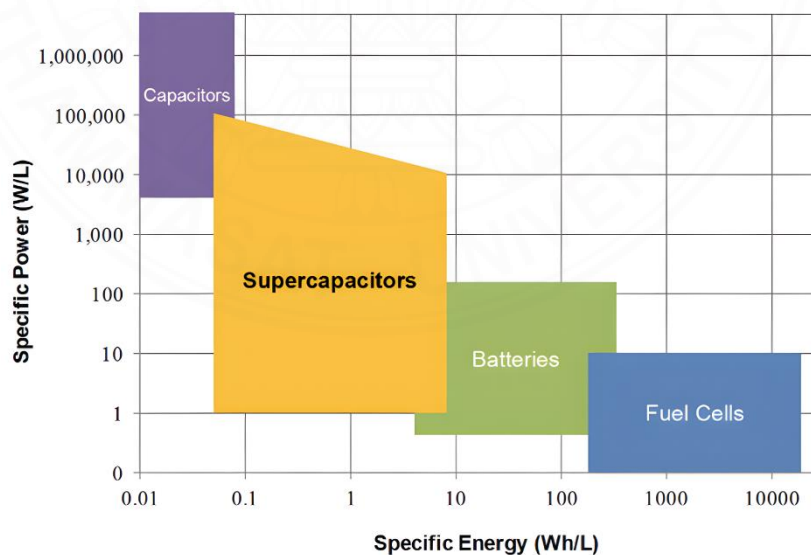


Figure 2.1 Ragone plot for different storage devices. Adapted from “Anode Material of Vanadium Nitride for Supercapacitors: A Topic Review”, Journal of Materials Chemistry A. (Y. Liu et al., 2020)

2.2 Supercapacitor

Supercapacitors are electrochemical energy storage devices with high power density and specific capacitance. These devices have the capacity to efficiently discharge high-density energy in a short period of time. Supercapacitors are classified into two categories based on their working principles: pseudocapacitance and electric double-layer capacitance. Carbon-based compounds worked well as supercapacitor electrode materials (Keçili, Arli, & Hussain, 2020).

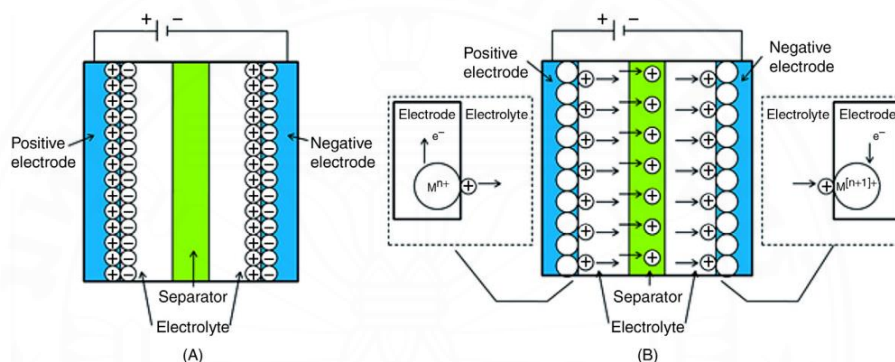


Figure 2.2 Schematic diagram of supercapacitors. (a) EDLC; (b) pseudocapacitor. Adapted from “NiCo₂O₄-based supercapacitor nanomaterials”, Nanomaterials. (C. Wang et al., 2017)

Based on their energy storage capacity, supercapacitors are classed as either electrochemical double layer capacitors (EDLC) or pseudocapacitors (as shown in Figure 2.2). Two-plate capacitors make up an EDLC capacitor. During the charging process of a supercapacitor, charge accumulation occurs at the interface between the electrode and the electrolyte. Electrical energy is stored as electrons move from the negative electrode to the positive electrode through an external circuit. Within the electrolyte, cations migrate toward the negative electrode, while anions migrate toward the positive electrode. Conversely, during the discharge process, electrons and ions flow in the opposite direction. As a result, no actual charge transfer takes place within the EDLC supercapacitor. The pseudocapacitors are shown in Figure 2.2 (b) with similar mechanism but involving faradaic processes rather than EDLC mechanism

(Castro-Gutiérrez, Celzard, & Fierro, 2020; Dai et al., 2021; Nasser, Tiantian, & Song, 2022; Zhang et al., 2022).

2.2.1 Electrode material

The electrode material is a critical component of a supercapacitor, as its type and quality directly influence key performance metrics such as storage capacity, operating voltage, and overall efficiency. Electrostatic interactions between the two electrodes determine the behavior of an EDLC. In contrast, the behavior of pseudocapacitors arises from rapid and reversible faradaic reactions taking place on the electrode surfaces. Common electrode materials include metal oxides, polymers, graphene, and activated carbon.

2.2.2 Electrolyte

Electrolyte is a component of the supercapacitor. The dielectric constant of the electrolyte determines the charge storage capacity of a typical capacitor. Because of the electrolyte, charging and discharging are possible. The kind and quality of the electrolyte has a considerable influence on supercapacitor capabilities. Solid, liquid, and quasi-solid-state electrolytes are the three types of electrolytes (Sharma & Kumar, 2020).

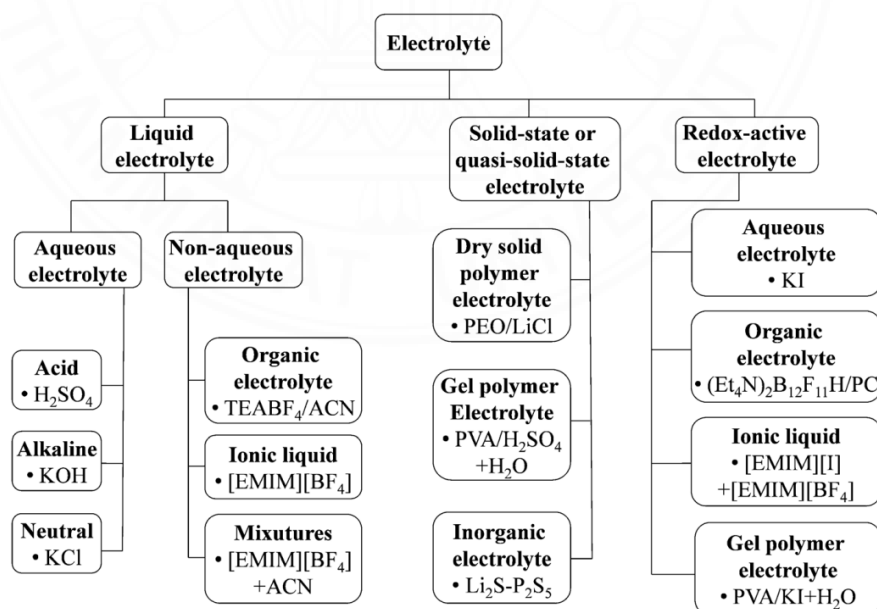


Figure 2.3 Types of electrolytes for supercapacitors. Adapted from “Study of electrode and electrolyte material of supercapacitor”, Materials Today: Proceedings. (Sharma & Kumar, 2020)

2.3 Activated carbon (AC)

Activated carbon (AC) has a long history of use in adsorbent technology, having been synthesized from a range of natural and synthetic precursors. It possesses a large surface area of around $1000 \text{ m}^2 \text{ g}^{-1}$ or more, extremely advanced porous structures, chemical inertness, and excellent mechanical stability (Heidarinejad et al., 2020). As a result, it is a desirable carbonaceous material for a wide range of environmental applications. Microcrystalline and nongraphitic carbon are the most frequent forms. The fundamental component of a carbonaceous material is carbon with the electrical configuration carbon. Carbon's unique capacity to make bonds with itself and other elements is owing to this arrangement, and it should be noted that this arrangement allows for the production of established structures such as pentagonal, hexagonal, heptagonal, etc (Adeleye et al., 2021; Sultana, Rownok, Sabrin, Rahaman, & Alam, 2022).

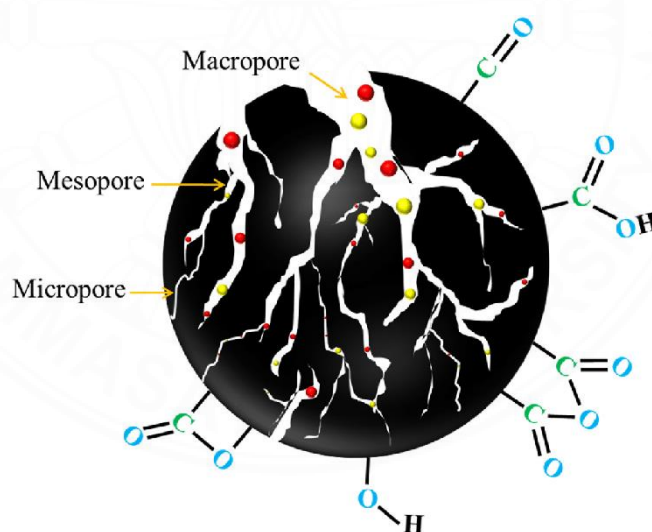


Figure 2.4 Schematic presentation of pore structure and surface functional groups of activated carbon. Adapted from “A review on experimental chemically modified activated carbon to enhance dye and heavy metals adsorption”, Cleaner engineering and technology. (Sultana et al., 2022)

AC can be produced either by directly activating a dry raw precursor or through a two-step process involving carbonization and activation. In the first stage, raw materials are carbonized at elevated temperatures, while the second stage involves heating to temperatures below 700°C in an oxygen-free environment, causing hydrocarbon species to be released through distillation. Additional activation methods can be employed to enhance porosity and develop solid cavities within the activated carbon structure. According to the International Union of Pure and Applied Chemistry (IUPAC), pores on support material surfaces are categorized into three types: micropores (less than 2 nm), mesopores (2–50 nm), and macropores (greater than 50 nm). Activated carbon can be manufactured using either physical or chemical processes (Adeleye et al., 2021; Castro-Gutiérrez et al., 2020; Sultana et al., 2022).

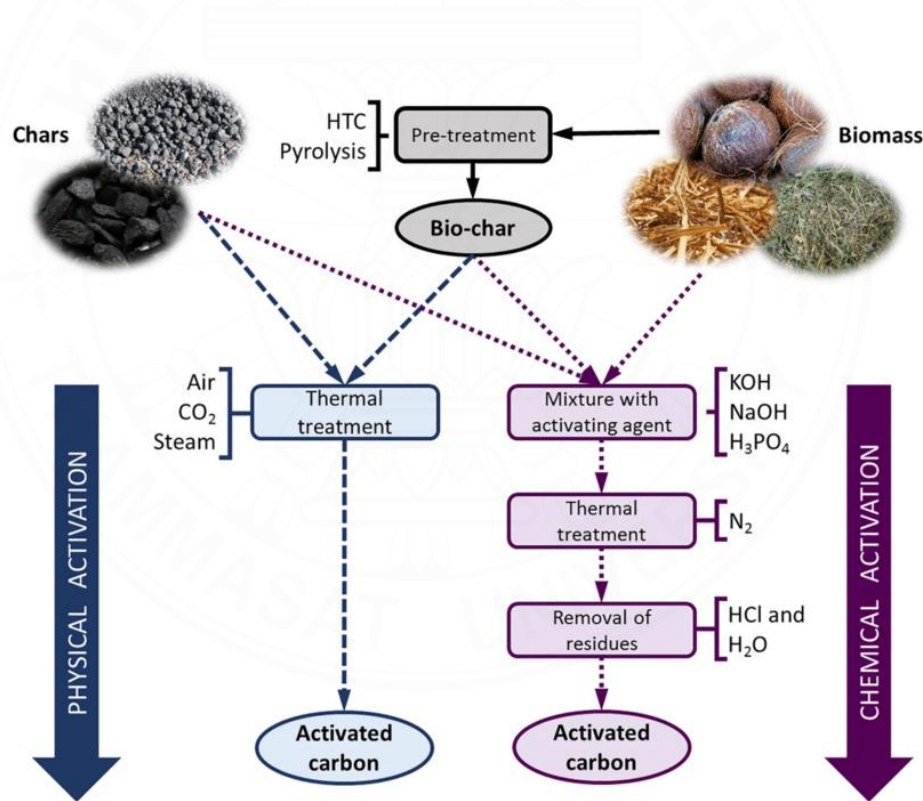
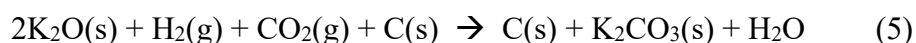
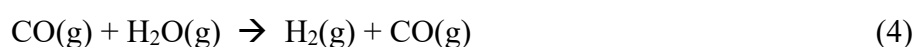
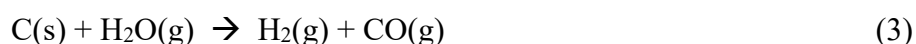
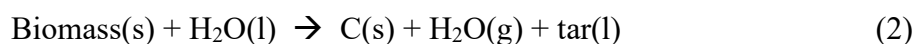


Figure 2.5 Schematic production process of activated carbons, from biomass and char, by physical or chemical activation. Adapted from “Energy storage in supercapacitors: Focus on tannin-derived carbon electrodes”, *Frontiers in materials*. (Castro-Gutiérrez et al., 2020)

Physical activation is a two-step process that involves carbonization in the atmosphere and activation in atmospheric oxidizing gases such as steam and carbon dioxide at temperatures 800-1100°C, whereas chemical activation is often utilized in biomass resources. The biomass can be activated directly or pre-treated to produce biochar. The precursors are impregnated with oxidizing and dehydrating chemicals in the first step. After impregnation, the suspension was dried, and the residual mixture was activated at temperatures of 400-900°C in an inert gas atmosphere in the presence of chemicals. Figure 2.5 shows how the activating chemicals can enter the carbon structure, resulting in the creation of microscopic holes in the activated carbon and an increase in surface area (Azmi, Buthiyappan, Raman, Patah, & Sufian, 2022; Castro-Gutiérrez et al., 2020).

The activation process enhances several surface properties of activated carbon, including surface area, porosity, pore volume, pore diameter, and surface functional groups. Activation techniques are classified into two main categories: physical and chemical activation. In physical activation, activating agents such as steam or carbon dioxide (CO₂) are utilized, whereas chemical activation involves the use of agents like ZnCl₂, KOH, K₂CO₃, and H₃PO₄, among others.

Chemical activation, particularly with activating agents such as KOH, is the most widely adopted method for producing activated carbon due to its simplicity and accessibility. The KOH activation process follows specific chemical reactions ((1), (2), (3), (4), (5)), during which the release of volatile species contributes to improving the microstructure of the activated carbon, as illustrated in Figure 2.6 (Hu et al., 2023; Singh et al., 2017).



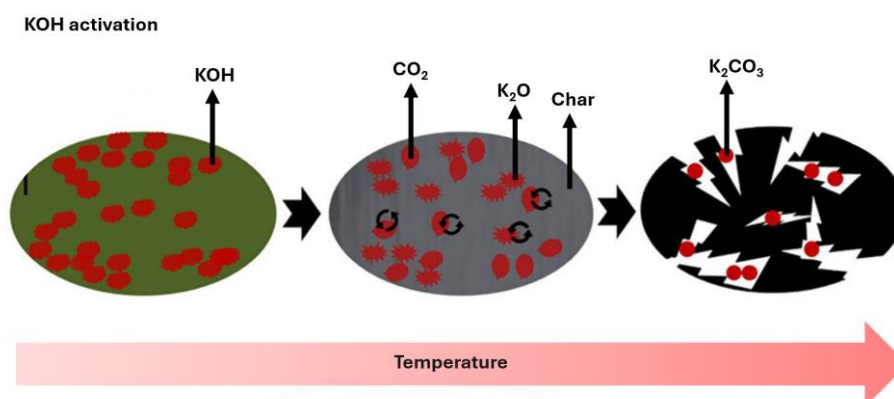


Figure 2.6 Schematic diagram of KOH activation process. Adapted from “Comparison of activated carbons prepared from wheat straw via ZnCl₂ and KOH activation”, Waste and biomass valorization. (Ma, 2017)

Table 2.1

Previous research on Hemp-derived activated carbon

Raw material	Activating agent	Activation conditions	S _{BET} (m ² g ⁻¹)	References
Hemp bast fiber	KOH	750°C, 1h in N ₂ atmosphere	2425	Hossain M. Z. et al, journal of carbon, (2018)
Sisal hemp	KOH	600°C, 2h in N ₂ atmosphere	1303.5	Tan Y. et al, Journal of Alloys and Compounds, (2020)
Hemp shives	KOH	550°C, 2h in N ₂ atmosphere	1990	Ivanichok N. et al, Physics and Chemistry of Solid State, (2020)
Deccan hemp core fiber	KOH	500°C, 1.15h in N ₂ atmosphere	237.1	Ajaya K. M. et al, AIP Publishing, (2020)

Previous research on Hemp-derived activated carbon (cont.)

Raw material	Activating agent	Activation conditions	S _{BET} (m ² g ⁻¹)	References
Hemp stem	NaOH	700°C, 2h in N ₂ atmosphere	2110.8	Zhang J. et al, Journal of Physics and Chemistry of Solids, (2021)
Hemp Hurd	K ₂ CO ₃	700°C, 1h in N ₂ atmosphere	266	Antorán D. et al, Energy & Fuels, (2023)

2.4 Modification of AC

Table 2.2

Advantages and drawbacks in the modification of AC (Malini, Selvakumar, & Kumar, 2023)

Advantages	Drawbacks
Enhancement of the lone pair of electrons that provide as Lewis bases	Byproducts of the modification reaction pollute the environment with chemicals
Textural characteristics like as surface area and pore volume are improved	Higher energy consumption because surface modification at high temperatures is required to integrate functional groups
Improvement in the carbon, nitrogen and oxygen contents	

2.4.1 Nitrogen doped AC

Nitrogen-containing groups in AC may appear in three distinct forms: pyridinic, pyrrolic, and graphitic, all of which enhance microporosity and surface area. Pyridinic-N atoms create hexagonal structures that are coupled to two carbon atoms, each of which provides one p electron. Pyrrolic-N atoms are sp³ hybridized to two

carbon atoms, giving two p electrons. Nitrogen is sp^2 hybridized and bound with three carbon atoms to form graphitic-N. Graphitic N may be found on the margins of graphitic carbon layers, whereas pyridinic and pyrrolic N are found within the graphitic carbon layer. AC also contains oxidized-N and aminic-N. To regulate the creation of these nitrogen species, the temperature of carbonization can be changed. Aminic-N is formed at temperatures above 300°C , whereas pyridinic and pyrrolic nitrogen are formed at temperatures above 600°C . The existence of graphitic nitrogen increases as the carbonization temperature goes over 700°C , whereas the amount of all other nitrogen species declines. Nitrogen doping in AC may be estimated using CHN and XPS analysis. By inserting a heteroatom into the carbon framework, nitrogen doping enhances surface characteristics by resulting in flaws and pores (Azmi et al., 2022; Hsu, Tu, Yang, Wang, & Hu, 2020; Malini et al., 2023).

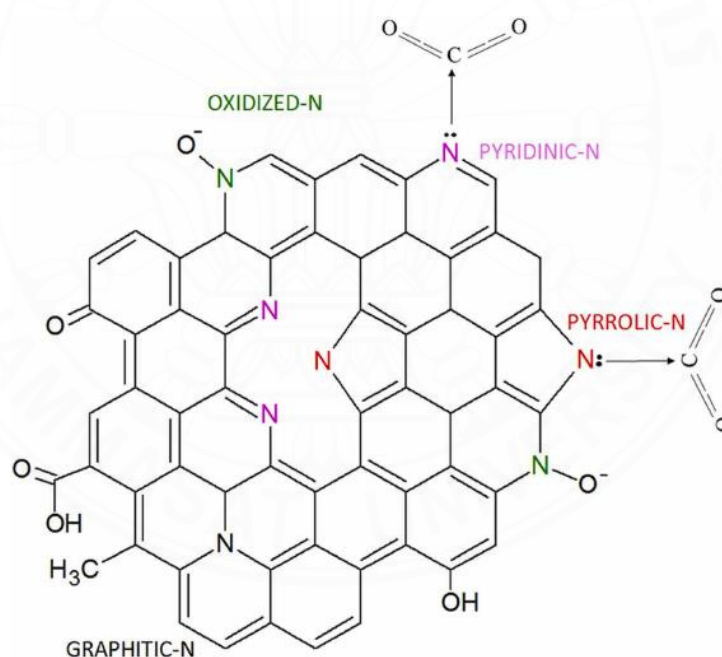


Figure 2.7 Structure of N-doped AC. Adapted from “Heteroatom functionalized activated porous biocarbon and their excellent performance for CO₂ capture at high pressure”, Journal of Materials Chemistry A (Singh et al., 2017)

2.4.2 Nitrogen, sulfur co-doped AC

In addition to single heteroatom doping, co-doping can improve electrode material performance. Furthermore, co-doping can improve the conductivity and surface area of the electrode material. As a result, the electrochemical charge storage properties can be enhanced. Through redox processes, other heteroatoms, such as B, P, or S atoms, contribute to the enhancement of capacitance in carbon-based materials. Charge storage in micro-scopic pores via EDLC is more effective due to the synergistic interaction of the N- and S-dopants and the potential of easier polarizability, sulfur, in particular, since sulfuric acid changes the charge on adjacent carbon atoms to a more positive state (Hu et al., 2023; Uppugalla, Pothu, Boddula, Desai, & Al-Qahtani, 2023).

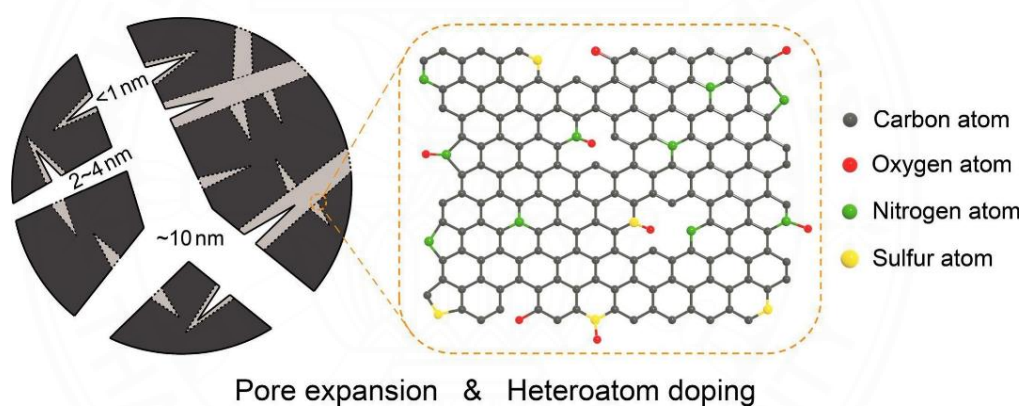


Figure 2.8 Structure and morphology of N, S-doped AC. Adapted from “Synthesis, analysis and characterization of nitrogen/sulfur co-doped activated carbon for high-performance all-printed flexible supercapacitor”, Journal of Energy Storage. (Hu et al., 2023)

2.5 Raw materials

2.5.1 Hemp

Hemp is a botanical class of *Cannabis sativa L.subsp. sativa* that are used for industrial or therapeutic purposes. The quantity of tetrahydrocannabinol (THC) in hemp and marijuana differs significantly. To be legal, hemp or hemp products require

less than 0.2-0.3% THC. Hemp is a strong, fragrant, annual plant. The slender cane-like stalks are hollow except at the tip and base. The leaves are palmately complex, with small greenish yellow blossoms. Pistillate, or female, plants have seed-producing blooms in tall spikelike clusters. Pollen-producing flowers on staminate, or male, plants form many-branched clusters.



Figure 2.9 Hemp from Encyclopaedia Britannica, (2023)

In temperate zones, hemp grows as an annual seed and may reach heights of up to 5 meters (16 ft). Crops thrive in sandy loam with excellent drainage and necessitate at least 65 mm (2.5 inches) of rain each month during the growing season.

Products and uses

Hemp is used in the production of various commercial and industrial products, including ropes, textiles, clothing, footwear, food, paper, bioplastics, insulation, and biofuels. While bast fibers can be processed into 100% hemp textiles, they are often blended with other materials such as linen, cotton, silk, or both virgin and recycled polyester. Additionally, hemp fibers are utilized in industrial applications such as mulch, animal bedding, and compost.

When hemp seed oil is oxidized (a process known as "drying"), it solidifies and can be used in the production of woven fabrics for clothing and furnishings. The inner fibers of the plant also have diverse applications, including the

production of oil-based paints, moisturizers, cooking oils, and biodegradable polymers (Deitch, 2003; Erickson, 2019; Keller, 2013; Süzerer, Tilkat, Onay, & Fidan, 2023; Tourangeau, 2015).

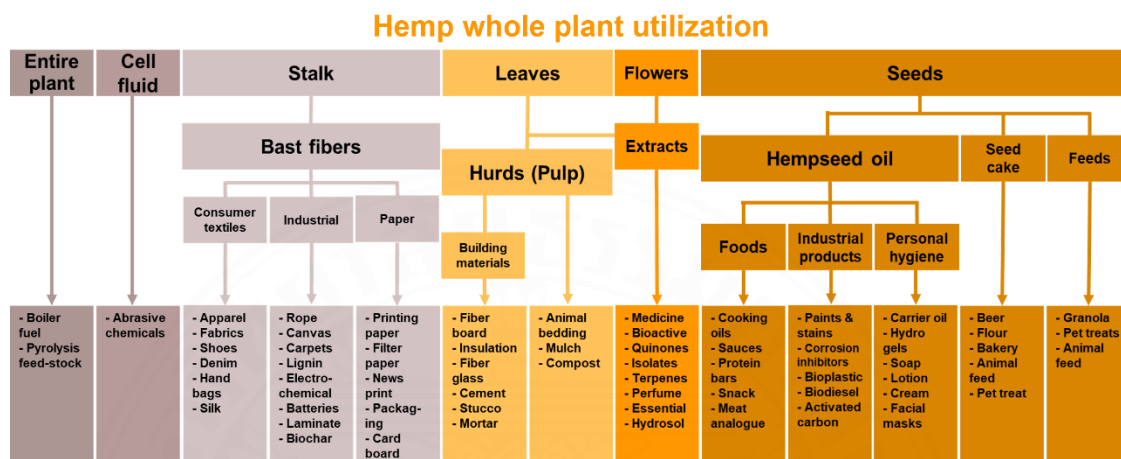


Figure 2.10 Products and uses of hemp from Krungsri research, (2021)

Hemp, a type of lignocellulosic biomass rich in carbohydrates, is abundant, cost-effective, and often underutilized. The primary chemical components of lignocellulosic materials include cellulose, hemicellulose, and lignin, along with smaller quantities of substances such as ash, proteins, lipids, waxes, and various extractives (table 2.3). Due to its high carbon content, the hemp core is a promising raw material for producing activated carbon, which can serve as an electrode material for supercapacitors. Recent studies, as summarized in Table 2.4, have explored the potential of hemp-derived activated carbon in EDLC applications (Gandolfi, Ottolina, Riva, Fantoni, & Patel, 2013).

Table 2.3

Chemical composition of hemp (Gandolfi et al., 2013; Thomsen, Rasmussen, Bohn, Nielsen, & Thygesen, 2005)

Chemical composition	Hemp stem	Hemp fibers	Hemp shives	Hemp core
Ash (%w/w)	-	4	1-2	1.2
Cellulose (%w/w)	70	55-72	34-44	44
Hemicellulose (%w/w)	22	7-19	31-37	25
Lignin (%w/w)	6	2-5	19-28	23
Pectin (%w/w)	-	4-8	4	0.6
Water sol. mat. (%w/w)	-	2	-	7
Fat and wax (%w/w)	-	0.7-1.3	1	0.8

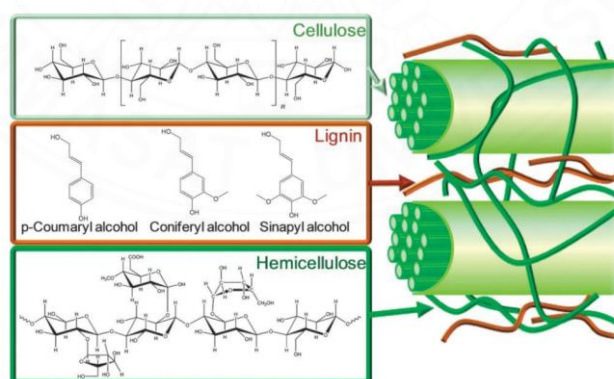


Figure 2.11 Chemical composition of plant. Adapted from “Green and sustainable route for oxidative depolymerization of lignin: New platform for fine chemicals and fuels”, Biotechnology Progress. (Sangeetha K. et al, 2021)

Table 2.4

Previous research on Hemp-derived activated carbon for EDLC applications

Raw material	Electrolyte	C_{sp} (F g ⁻¹)	S_{BET} (m ² g ⁻¹)	Cyclic stability	References
Hemp stem	6M KOH	318	3062	96%, 10,000 cycles	Wang Y. et al, Industrial Crops and Products, (2015)
Hemp fiber	1M H ₂ SO ₄	122	673	-	Mijailović D. et al, Journal of The Electrochemical Society, (2017)
Hemp straw	6M KOH	279	865	91.6%, 5000 cycles	Jiang X. et al, Ionics, (2019)
Deccan hemp core fiber	1M KOH	51	237	70%, 5000 cycles	Ajaya K. M. et al, AIP Publishing, (2020)
Hemp fiber	PVA-KOH hydrogel	457	1060	85%, 10,000 cycles	Gunasekaran, S. S. et al, Journal of Energy Storage, (2021)

* C_{sp} = Specific capacitance**2.5.2 Pyroligneous acid**

Pyroligneous acid (PA) is a complex, oxygen-rich aqueous liquid derived from the condensation of vapors generated during the thermochemical decomposition or pyrolysis of plant biomass components, including cellulose, hemicellulose, and lignin. Typically, PA appears as a yellowish-brown to dark-brown liquid, produced through the slow pyrolysis of plant-based materials, as illustrated in Figure 2.11 (Mathew & Zakaria, 2015).



Figure 2.12 Color of pyroligneous acid from pyrotech energy.

PA is a highly oxygenated organic liquid, crudely condensed as a byproduct of plant biomass pyrolysis. Its composition primarily includes aliphatic, aromatic, and naphthenic hydrocarbons, along with various oxygenated compounds such as alcohols, aldehydes, ketones, furans, acids, phenols, and ethers. PA exhibits antioxidant and scavenging properties, making it valuable in applications such as antibacterial agents, insecticides, fertilizers, and enhancers of plant growth in agricultural practices.

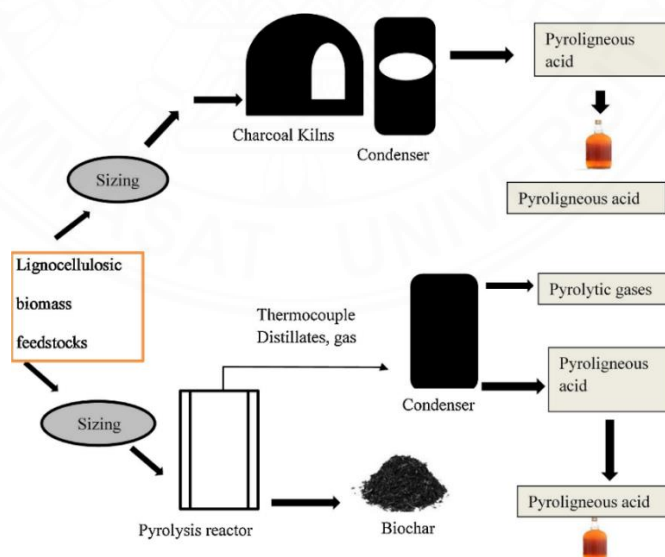


Figure 2.13 Production of pyroligneous acid. Adapted from “production, prospects and potential application of pyroligneous acid in agriculture”, Journal of analytical and applied pyrolysis. (Grewal, Abbey, & Gunupuru, 2018)

PA is a byproduct of burning charcoal. The charcoal burning process by local agricultural people consists of 4 main steps (Khlangsap, Tara, & Jamornchotisin, 2011):

1. The process of eliminating moisture begins when the stove is lit, causing the temperature to steadily rise. At approximately 150°C, smoke begins to form within the furnace, and as the temperature climbs to 200-250°C, the smoke emits a strong, pungent odor. This moisture removal phase typically spans 2-3 hours from the moment the stove is ignited.

2. The method of converting wood into charcoal when the stove's headlight is left on indefinitely. The temperature inside the stove will increase to around 300-400°C, and smoke will accumulate densely. The growth is hazy white and stinks strongly. During this phase, the wood begins to char and undergoes an exothermic reaction. The furnace's temperature will continue to climb. Then, take the acid-resistant pipe placed above the chimney's mouth to capture the smoke. Finally, the smoke cools, condenses, and forms water droplets. The collection duration of PA will be roughly 4 hours from the start of collection, or if the color of the smoke at the furnace begins to become blue, cease collecting wood vinegar.

3. To purify charcoal, begin by opening the front of the furnace to facilitate airflow, intensifying the heat for burning, and eliminating tar from the charcoal. This process raises the temperature in front of the furnace to over 150°. It is crucial not to store PA at this time due to its harmful compounds. Turn off the furnace when the smoke changes from blue to clear.

4. To cool down and prepare charcoal, allow the furnace to cool gradually. Prior to opening it, ensure the temperature inside the furnace is below 50°C to prevent accidental ignition of the charcoal. The initial step upon opening is to open the chimney to release any remaining heat and gases from the furnace. Subsequently, proceed to open the front of the furnace.

PA is a complex substance characterized by a high concentration of carbon and oxygen molecules. Table 2.5 provides a detailed summary of the various elemental components of PA, as well as the physicochemical properties associated with wood-derived PA (Grewal et al., 2018; Jahanban-Esfahlan & Amarowicz, 2018; Li et al., 2021; Yuan et al., 2022).

Table 2.5*Properties of PA (Grewal et al., 2018)*

Properties	Value in PA
Moisture content (wt %)	15-30
pH	2.5
Specific gravity	1.2
Elemental composition (wt%)	Value in PA
C	54-58
H	5.5-7.0
O	35-40
N	0-0.2
Ash	0-0.2
High heating value (MJ/Kg)	16-19
Viscosity at 773 K (cP)	40-100
Total solids (wt %)	0.2-1.0
Distillation residue (wt %)	Up to 50

Table 2.6*Chemical composition of PA from GC-MS analysis (Zhai et al., 2015)*

Chemical class	Compounds
Ketones	Cyclopentanone
	Dihydro-2-methyl-3(2H)-furanone
	3-Hydroxy-2-butanone
	1-Hydroxy-2-propanone
	2-Cyclopenten-1-one
	4-Hydroxy-4-methyl-2-pentanone
	2-Methyl-2-cyclopenten-1-one
	1-Hydroxy-2-butanone
	3,4-Dimethyl-2-cyclopenten-1 one
	1-(2-Furanyl)-ethanone
	3-Methyl-2-cyclopenten-1-one
	Dihydro-5-methyl-2(3H)-furanone
	2,5-Dihydro-3,5-dimethyl-2-furanone
	2(5H)-furanone
	3-Methyl-1,2-cyclopentanedione
	3-Ethyl-2-hydroxy-2-cyclopenten-1-one
Aldehydes	1-(4-Hydroxy-3-methoxyphenyl)-2-propanone
	1-(4-Hydroxy-3,5-dimethoxyphenyl)-ethanone
	Furfural
	5-Methyl-2-furancarboxaldehyde
Esters	1H-pyrrole-2-carboxaldehyde
	4-hydroxy-3,5-dimethoxy-benzaldehyde
	4-hydroxy-2-methoxycinnamaldehyde
Esters	Ethyl acetate
	4-Oxo-pentanoic acid methyl ester
	1,2-Ethanediol-dipropionate
	Butyrolactone

Chemical composition of PA from GC-MS analysis (Cont.)

Chemical class	Compounds
Esters	Methyl 4-hydroxybutanoate
	Pentanedioic acid monomethyl ester
	4-Hydroxy-3-methoxy-benzoic acid methyl ester
Alcohol	2-Furanmethanol
Phenol and derivatives	2-Methoxy-phenol
	2-Methoxy-5-methyl-phenol
	2-Methoxy-4-methyl-Phenol
	Phenol
	4-Ethyl-2-methoxy-phenol
	4-Methyl-phenol
	2-Methoxy-4-propyl-phenol
	2,6-Dimethoxy-phenol
	5-Tert-butylpyrogallol
	3-Methoxy-1,2-benzenediol
	3-Methoxy-5-methyl-phenol
	2,6-Dimethoxy-4-(2-propenyl)-phenol
	1,2-Benzenediol
	2-Methoxy-4-(methoxymethyl)-phenol
	2-Methyl-1,4-benzenediol
	Desaspidinol
	Hydroquinone
Benzene derivations	1,2,3-Trimethoxy-5-methyl-benzene
	1,2,4-Trimethoxybenzene
	4-Hydroxy-3,5-dimethoxy-benzoic acid hydrazide
	Methyl-(2-hydroxy-3-ethoxy-benzyl)ether
Organic acids	Acetic acid
	Formic acid
	Propanoic

Chemical composition of PA from GC-MS analysis (Cont.)

Chemical class	Compounds
Organic acids	Tetradecanoic acid
	n-Hexadecanoic acid
	Octadecanoic acid



CHAPTER 3

RESEARCH METHODOLOGY

3.1 Materials and chemicals

The hemp cores and pyroligneous acid were procured from a Thai hemp plantation. All analytical quality compounds were acquired from Sigma-Aldrich, and all analytical grade chemical solvents were purchased from Carlo Erba Reagents. As a current collector, carbon paper was utilized.

3.2 Synthesis of electrode materials

3.2.1 Hemp-derived activated carbon (HAC)

The dried hemp cores were crushed into 200 mesh powder. In a Teflon-lined autoclave, 5 g of the powdered hemp cores were mixed with 100 mL of 1 M phosphoric acid (H_3PO_4) and heated at 200°C for 5 hours. After cooling to room temperature, the resulting material was repeatedly rinsed with distilled water until it reached a neutral pH, followed by filtration to isolate the carbon char, which was then dried overnight at 80°C.

The obtained carbon char was utilized to produce activated carbon. In the presence of 60 mL of deionized water, the carbon char was treated with potassium hydroxide (KOH) as an activating agent in a 1:1 ratio. This mixture was stirred continuously and heated to 80°C until a slurry formed. The slurry underwent activation in a tube furnace under nitrogen gas for 2 hours, with the temperature ramped at 10°C/min to 800°C and at 5°C/min to 700°C for comparison. Post-activation, the material was washed several times with 1 M hydrochloric acid (HCl) and hot deionized water until a neutral pH was achieved, then dried in an oven at 80°C for 24 hours.

3.2.2 Hemp-derived N, S co-doped activated carbon (N, S-HAC)

Following the carbon char preparation steps outlined above, in the presence of DI water (60 mL), the carbon char was impregnated with KOH as an activating agent (ratio 1:1) and the synthesis for classifying AC by adding thiourea via the activation process in various ratios is shown in Table 3.1. The mixture was then heated to 80°C with constant stirring until it formed a slurry. The slurry was then

activated at 700°C and 800°C under the same circumstances. After activation, it was washed multiple times with 1 M HCl and hot DI water until a neutral pH was obtained, then dried in an oven at 80°C for 24 hours.

Table 3.1

Different types of activated carbon

Sample	Activation process	Activation temperature (°C)	Thiourea amount (%wt)
AC800-1	undoped		0
AC800-2	10% wt	800°C	10
	thiourea doped	at heat rate	
AC800-3	20% wt	10°C/min	20
	thiourea doped		
AC1-700	undoped		0
AC2-700	10% wt	700°C	10
	thiourea doped	at heat rate	
AC3-700	20% wt	5°C/min	20
	thiourea doped		

3.3 Fabrication of electrodes

The produced HAC, carbon black (CB), and poly(vinylidene fluoride) (PVDF) served as the active material, conductive agent, and binder, respectively, and were mixed in a weight ratio of 80:15:5% using N-methyl pyrrolidone (NMP) as the solvent. The resulting mixture was applied onto carbon paper, functioning as the current collector, and dried in an oven at 50°C overnight. Circular electrodes with a 1 cm diameter were then fabricated for use in a Swagelok cell.

3.4 Electrolyte preparation

Pyroligneous acid was centrifuged at a speed of 10,000 rpm at 25°C for 15 minutes and then KOH at a concentration of 1, 2, 3, 5 and 6 molars were added to pyroligneous acid and stir until completely dissolved to obtain a KOH/PA electrolyte.

3.5 Characterization

Through a Belsorp Max Analyzer, the nitrogen adsorption-desorption experiment was carried out to estimate the specific surface area, pore size, and pore volume. The Brunauer-Emmett-Teller (BET) technique was used to calculate the specific surface area, the Non-Local Density Functional Theory/Grand Canonical Monte Carlo (NLDFT/GCMC) method was used to calculate the pore volume and pore size distribution, and X-ray photoelectron spectroscopy (XPS, AXIS Ultra DLD). To analyze the crystallinity/amorphous nature, an X-ray diffraction (XRD) examination was done utilizing the RigakuD/max2550VL/PC system. Morphological characterization by Scanning electron microscope (SEM, BenchTop-SEM (JEOL, JCM-6000)). Contact angles were measured using a tensiometer (100 Theta Lite, Biolin Scientific) with 1 μ L of electrolyte droplet.

3.6 Electrochemical measurements

Electrochemical characterizations were conducted using a potentiostat/galvanostat (μ Autolab, PGSTAT204). Two types of electrochemical cells were employed: (a) a three-electrode configuration with AC/CB/PVDF as the working electrode, platinum (Pt) as the counter electrode, and an Ag/AgCl reference electrode, and (b) a two-electrode system consisting of symmetric AC/CB/PVDF electrodes. The three-electrode setup was used for cyclic voltammetry (CV) and galvanostatic charge-discharge (GCD) measurements, while the two-electrode system was utilized for electrochemical impedance spectroscopy (EIS) and cyclic stability tests.

CV and GCD tests were performed in KOH and KOH/PA electrolytes within a potential window of 1 V, with scan rates ranging from 5 to 100 mV s⁻¹ and

current densities from 2 to 4.5 A g⁻¹. Cyclability was evaluated using a Swagelok cell, which incorporated Whatman filter paper as the separator and 1 cm diameter carbon paper as the current collector.

3.7 Calculations

The specific capacitance (C_{sp}) values can calculate from the equation above:

$$C_{sp} = \frac{I\Delta t}{m\Delta V} \quad (\text{Eq.1})$$

$$C_{sp} = \frac{\int I dv}{2mv\Delta V} \quad (\text{Eq.2})$$

where C_{sp} is the specific capacitance in F g⁻¹, I is the average current in A, m is the mass of the material in g, S is the scan rate in V s⁻¹, Δt is the time in s, and ΔV is the potential window in V.

The energy density and the power density:

$$E = \frac{C_{sp}(\Delta V)^2}{2} \quad (\text{Eq.3})$$

$$P = \frac{E}{t} \quad (\text{Eq.4})$$

where E is energy density in Wh kg⁻¹, P is power density in W kg⁻¹, and t is the discharge time in hour.

Analysis of capacitance contributions: Dunn's method

$$i(v) = k_1 v + k_2 v^{1/2} \quad (\text{Eq.5})$$

$$\frac{i(v)}{v^{1/2}} = k_1 v^{1/2} + k_2 \quad (\text{Eq.6})$$

where k_1 is surface capacitive coefficient and k_2 is diffusion coefficient, which are calculated from slope and interception between $\frac{i(v)}{v^{1/2}}$ and $v^{1/2}$, respectively.

CHAPTER 4

RESULTS AND DISCUSSION

4.1 Synthesis and characterization of AC800

In this study, activated carbon derived from hemp cores was employed as an electrode material in conjunction with a 3 M KOH electrolyte for assembling supercapacitors. Different content of thiourea resulted in the creation of 3 types of AC800. KOH was utilized as the activating agent to enhance surface properties such as surface area, porosity, pore volume, and pore diameter.

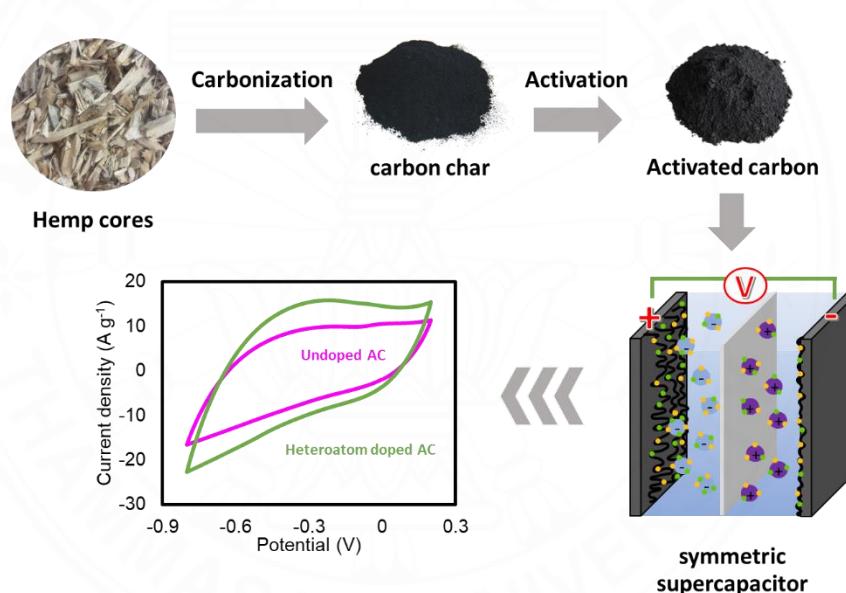


Figure 4.1 Schematic of hemp-based supercapacitor.

The specific surface area (S_{BET}) and pore size distribution were determined through N_2 adsorption and desorption analysis. Figure 4.2 (a) shows the N_2 adsorption and desorption isotherm results for the samples, highlighting that AC800-3 exhibits the highest surface area of $1853 \text{ m}^2 \text{ g}^{-1}$ and a pore volume of $0.60 \text{ cm}^3 \text{ g}^{-1}$. The isotherm observed in Figure 4.2 (a) demonstrates characteristics of type I and IV adsorption isotherms. This classification indicates the presence of mesopores, which play a significant role in enhancing charged ion transport and improving electrochemical properties (Raj, Jaya, Boopathi, Kalpana, & Pandurangan, 2020). Furthermore, Figure

4.2 (b) illustrates the associated pore size distributions investigated using the BJH system. The XRD pattern shown in Figure 4.2 (c) obtained from the generated AC represents its structural composition and degree of graphitization. The pattern reveals an amorphous phase, noticeable through a prominent peak between $2\theta = 18\text{--}29^\circ$, and a faint, broad peak at $41\text{--}45^\circ$, corresponding to the (002) and (100) planes respectively. The existence of the (100) plane signifies the amorphous nature of the carbon, while the intensity of the (002) peak serves as an indicator of the extent of graphitization. (Raj, Boopathi, Kalpana, Jaya, & Pandurangan, 2022). Figure 4.2 (d) presents the Raman spectrum of AC800, showing two distinct peaks at 1320 and 1607 cm^{-1} , corresponding to the D band representing disordered carbon and the G band representing graphitic carbon. The I_D/I_G ratios for AC800-1, AC800-2, and AC800-3 are 4.07, 1.85, and 2.23, respectively. From these results, a decrease in the I_D/I_G ratio indicates a high defect density, reflecting a transition to a more amorphous carbon structure indicates that the material has undergone significant structural changes. This can be due to processes such as oxidation or reduction, which alter the sp^2 and sp^3 hybridization in the carbon structure (Childres, Jauregui, Park, Cao, & Chen, 2013). Although doping with nitrogen (N) and sulfur (S) using thiourea does not successfully incorporate these elements into the structure due to the high activation temperature and rapid heating rate, excessive doping helps reduce defects and remains more effective than no doping.

Scanning Electron Microscopy (SEM) is used to investigate the surface morphology and structural characteristics of AC. AC800-1 in Figure 4.3 (a) reveals a relatively smooth surface with some visible pores and cracks suggest a partially porous structure but with lower apparent surface roughness compared to the others. AC800-2 in Figure 4.3 (b) displays a more porous and irregular surface with abundant pore networks. The enhanced porosity indicates better textural development, possibly favorable for adsorption applications. AC800-3 in Figure 4.3 (c) exhibits a highly irregular structure with significant pore interconnectivity. This suggests extensive activation, leading to increased porosity and surface area.

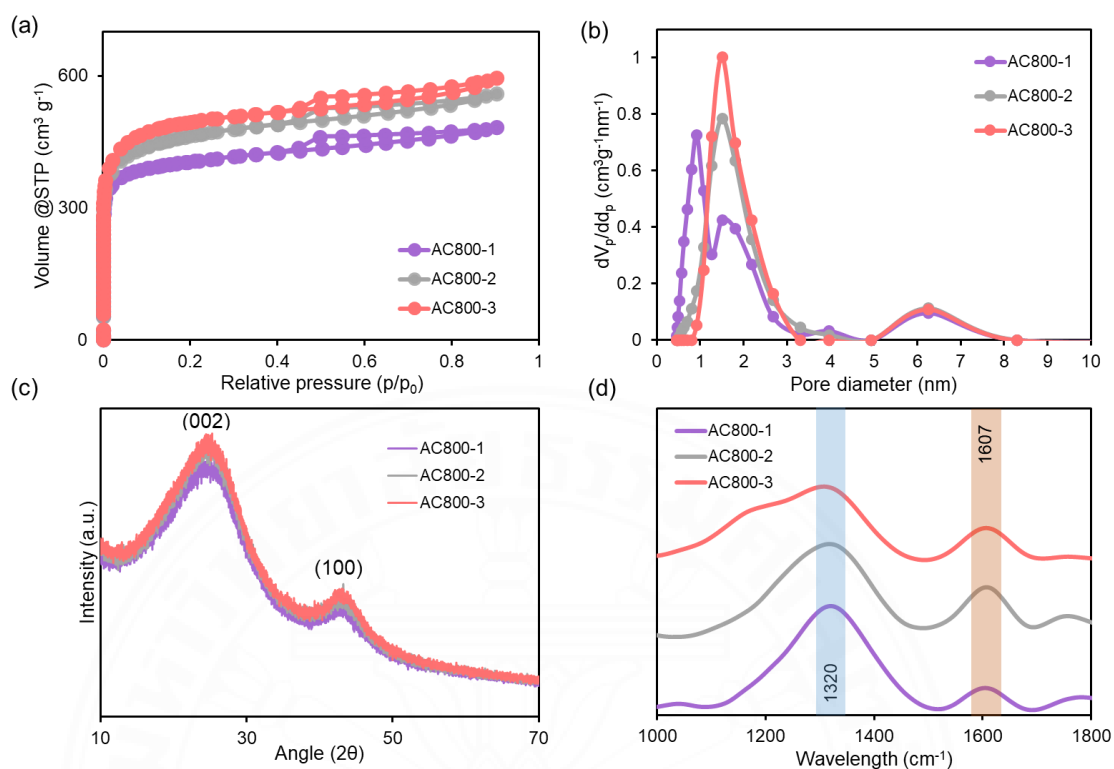


Figure 4.2 (a) N_2 adsorption-desorption isotherm, (b) pore-size distributions, (c) XRD patterns, and (d) Raman spectrum of AC800

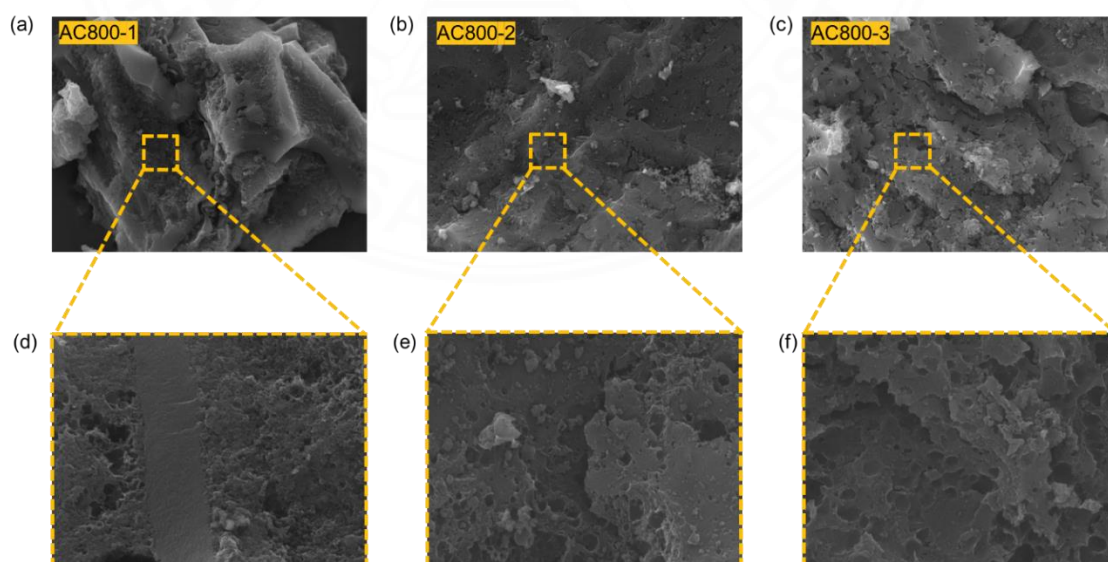


Figure 4.3 (a,d) SEM image of AC800-1, (b,e) SEM image of AC800-2, and (c,f) SEM image of AC800-3

The AC800 sample underwent elemental composition analysis using X-ray photoelectron spectroscopy (XPS). The survey XPS spectrum of AC800 (Fig. 4.4) revealed strong signals at 285 and 533 eV, corresponding to C_{1s} and O_{1s} . The atomic concentration is shown in table 4.1. The high-resolution of C_{1s} spectrum (Fig. 4.5 (a,c,e)) indicated distinct peaks attributed to C=C (285), C–O (286), C=O (287), and O–C=O (289) functional groups. High-resolution O_{1s} (Fig. 4.5 (b,d,f)) exhibited peaks related to C=O (531), O–C–O (532), C–OH (534), and C=O aromatic (535) groups, discernible upon deconvolution (Dai et al., 2021; Muthuraj, Ghosh, Kumar, & Mitra, 2019).

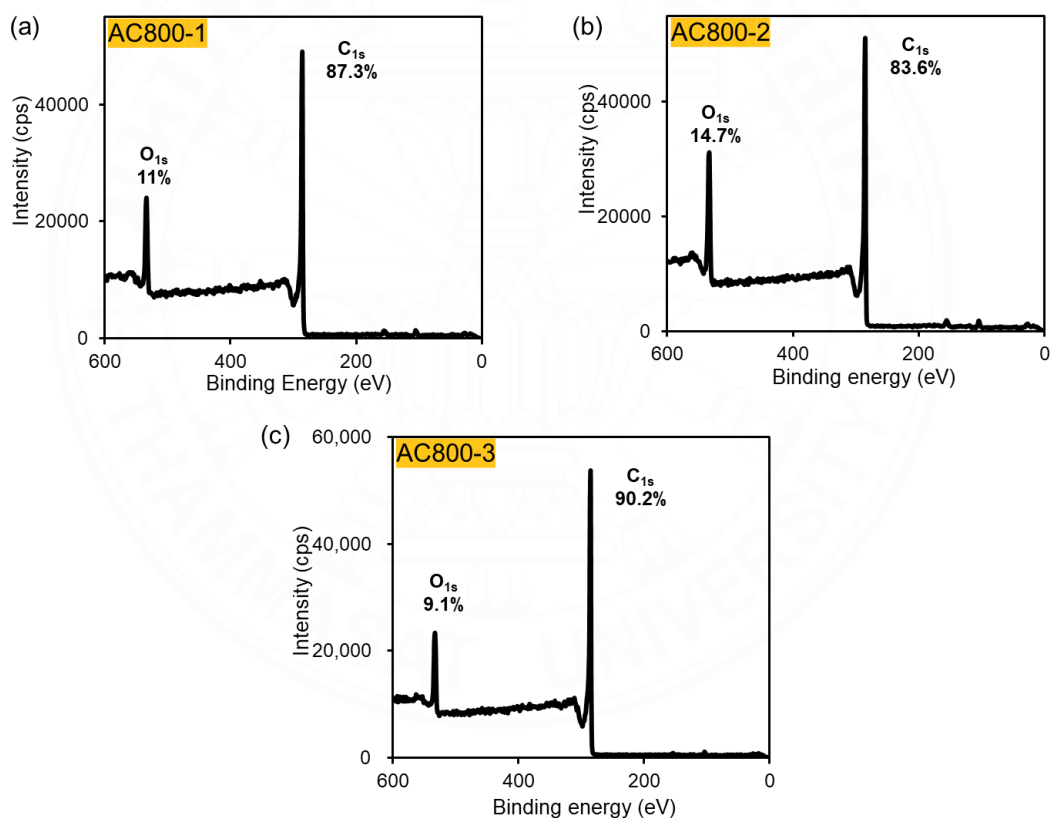


Figure 4.4 The survey XPS spectrum of AC800 (a) AC800-1, (b) AC800-2, and (c) AC800-3

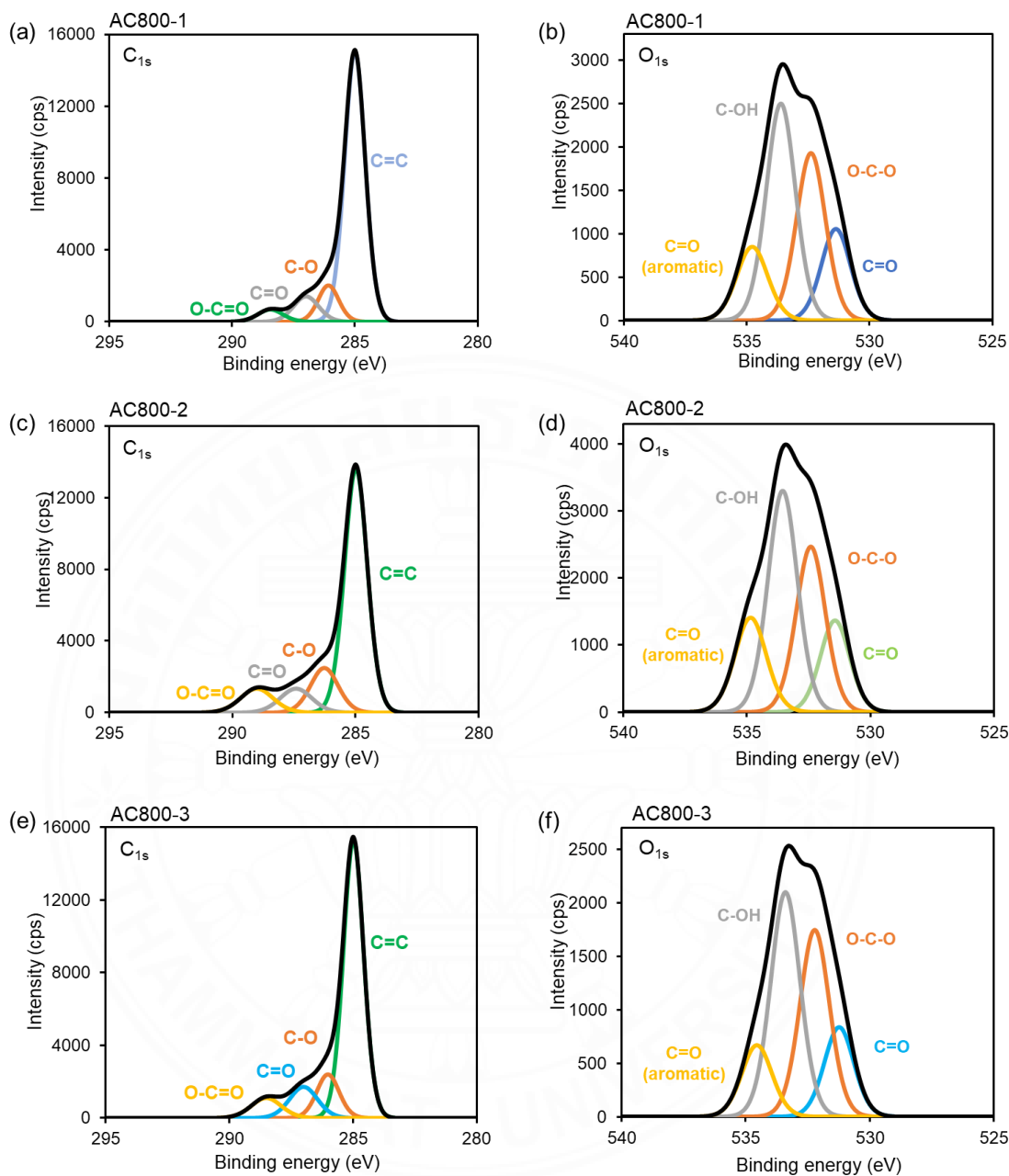


Figure 4.5 (a) high-resolution spectra C_{1s} of AC800-1, (b) high-resolution spectra O_{1s} of AC800-1, (c) high-resolution spectra C_{1s} of AC800-2, (d) high-resolution spectra O_{1s} of AC800-2, (e) high-resolution spectra C_{1s} of AC800-3, and high-resolution spectra O_{1s} of AC800-3

Table 4.1*The characterization of AC800*

Sample	Specific surface area (m ² g ⁻¹)	Pore volume (cm ³ g ⁻¹)	Pore diameter (nm)	Atomic concentration (%)			
				C	O	N	S
AC800-1	1547	0.39	1.75	87.25	11.05	-	-
AC800-2	1574	0.53	1.71	83.55	14.68	-	-
AC800-3	1853	0.60	1.60	90.19	9.11	-	-

4.2 Synthesis and characterization of AC700

The activated carbon derived from hemp cores was used as an electrode material. After hydrothermal hemp char was obtained and the activation processes were divided into 2 types: doping N, S by thiourea and undoping by using KOH as the activating agent.

On the assumption of N₂ adsorption and desorption, the specific surface area (S_{BET}) and pore size distribution are determined. The N₂ sorption isotherm results for the samples are shown in Figure 4.6 (a). Table 4.2 summarizes the surface behavior of the produced samples, including surface area and pore volume. Thus, AC700-2 has the highest surface area of 1663 m² g⁻¹ and a pore volume of 0.33 cm³ g⁻¹, respectively. Based on the results in Figure 4.6 (a), the isotherm is classified as type I and IV adsorption isotherms, indicating the presence of micropores and mesopores confirmed by pore size distribution, analyzed using the BJH method, is shown in Figure 4.6 (b). These pores enhance charged ion transport and improve electrochemical properties (Raj et al., 2020; Winata, Devianto, & Susanti, 2021).

The XRD pattern of the produced AC in figure 4.6 (c) is a reflection of its structural composition and graphitization level. The presence of the (100) plane indicates the carbon's amorphous nature, while the intensity of the (002) peak indicates the degree of graphitization (Raj et al., 2022). Figure 4.6 (d) presents the Raman spectrum of AC700, showing two distinct peaks at 1331 and 1603 cm⁻¹, corresponding

to the D band representing disordered carbon and the G band representing graphitic carbon. The I_D/I_G ratios for AC700-1, AC700-2, and AC700-3 are 1.41, 1.60, and 1.69, respectively. These results indicate that a higher amount of thiourea doping leads to an increase in the I_D/I_G ratio (Lin et al., 2024), reflecting the lower degree of graphitization of carbons. Activated carbon with a lower degree of graphitization exhibits a more disordered and porous structure, which is ideal for providing a higher surface area for energy storage applications. This structural characteristic enhances ion adsorption and storage capacity, making it suitable for supercapacitor electrodes (Ji, Wang, Yu, Wang, & Zhao, 2020). Confirmed by XRD pattern AC700-1 shows the highest degree of graphitization at high intensity of (002) peak (Chen et al., 2018).

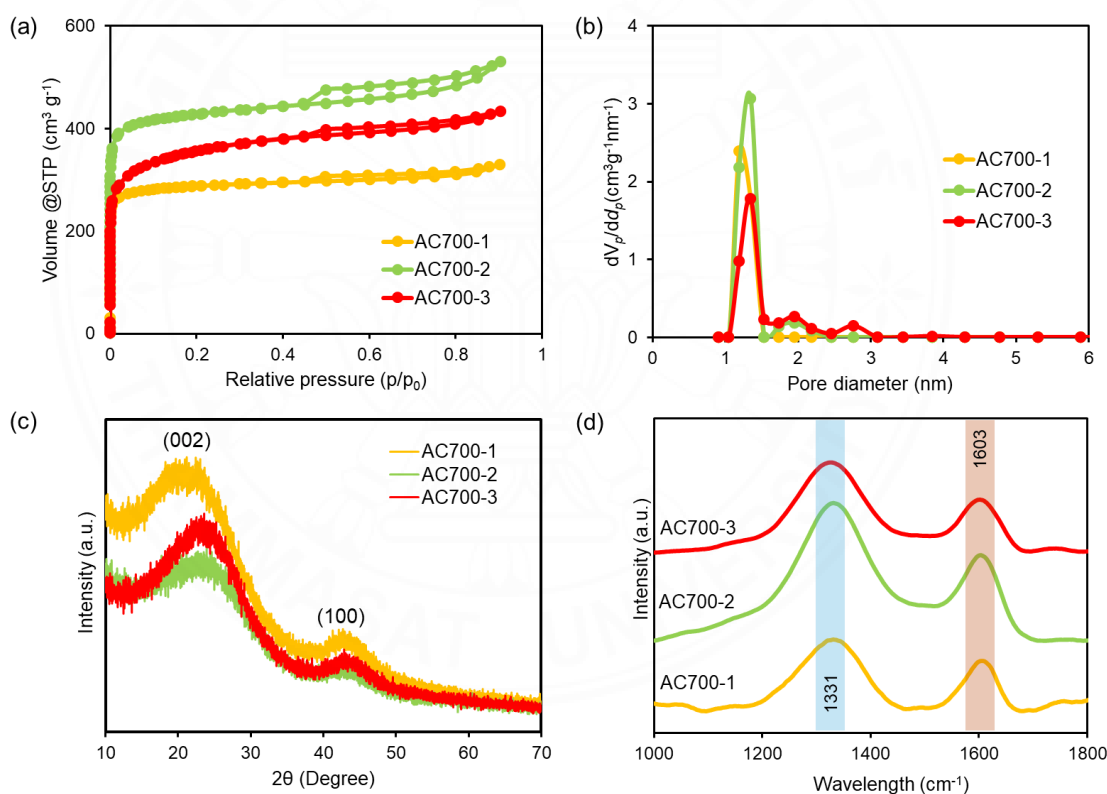


Figure 4.6 (a) N₂ adsorption-desorption isotherm and (b) pore-size distributions (c) XRD patterns, and (d) Raman spectra of AC700

The structural characteristics and surface morphology of materials are crucial for supercapacitor applications as they significantly affect the interaction

between the electrode and electrolyte. The SEM image of AC700-1, shown in Figure 4.7 (a), indicates a porous sheet-like morphology. The SEM image of AC700-2 confirms the development of an interconnected porous sheet morphology with numerous voids formed between the overlapping sheets of the sample, which could serve as ion buffer reservoirs. The uniform pore distribution highlights effective activation processes. On the other hand, AC700-3 with highest amount of thiourea shows the structure with fewer large particles. This irregular morphology might be due to excessive activation or structural collapse at high temperatures and high thiourea amount.

The formation of carbon sheet-like structures is attributed to the hydrothermal pre-carbonization step in a 1 M H_2SO_4 solvent, which acts as a mechanism for producing AC700-2 nanosheets through hydrothermal carbonization reactions and high-temperature KOH activation. This process reduces the crystallinity of cellulose and enhances the porosity of the biomass waste. Additionally, the penetration of KOH between the layers during chemical activation at 700°C with heating rate of $5^\circ\text{C}/\text{min}$ leads to the delamination into single or few-layer sheets. Furthermore, the reaction with thiourea facilitates the incorporation of heteroatoms (N and S), which act as defects, while thermal decomposition creates additional porosity in the carbon framework (Dubey, Maheshwari, Shrivastav, & Sundriyal, 2023).

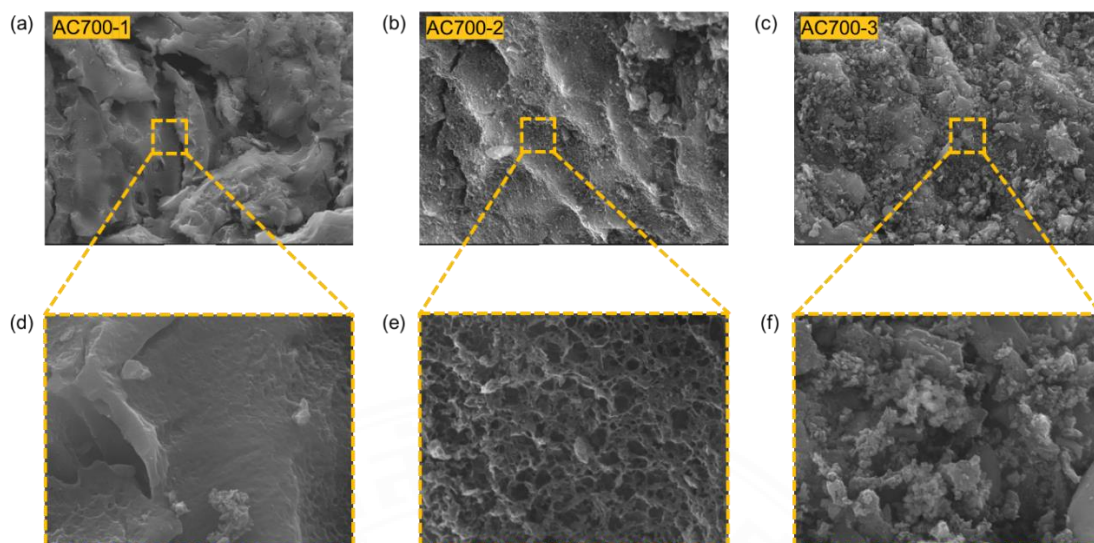


Figure 4.7 (a,d) SEM image of AC700-1, (b,e) SEM image of AC700-2, and (c,f) SEM image of AC700-3

Different specific surface area, pore volume, and pore diameter depend on the concentration of thiourea as shown in the elemental composition from the XPS in table 4.2. The survey XPS spectrum (Fig. 4.8) revealed strong signals at 533, 401, 285 and 169 eV, corresponding to O_{1s} , N_{1s} , C_{1s} and S_{2p} , respectively. From AC700-2, the high-resolution XPS spectrum of C_{1s} (Fig. 4.9 (a)) indicated distinct peaks attributed to C–C, C=C (285), C–N (286), C–O (287), C=O (288), and O–C=O (289) functional groups (Lee et al., 2017). High-resolution N_{1s} (Fig. 4.9 (b)) represent N-5 (Pyridinic N) (400) and N-6 (Pyrrolic N) (402) (Thumkaew et al., 2022). The presence of Pyridinic N is to enhance the charge storage capacity through its involvement in redox reactions, which can facilitate electron transfer during charge/discharge cycles (F. Liu, Niu, Chuan, & Zhao, 2023). Pyrrolic N also contributes positively to the electrochemical performance by providing additional active sites for charge storage (Yang & Zhou, 2017). High-resolution O_{1s} (Fig. 4.9 (c)) exhibited peaks related to C=O (531), O–C–O (532), C–OH (533), and C=O aromatic (535) groups. The S_{2p} high-resolution spectrum (Fig. 4.9 (d)) was characterized by doublets within the $S_{2p_{3/2}}$ (169) to $S_{2p_{1/2}}$ (170) region. Moreover, from high-resolution N_{1s} of AC700-3 shows graphitic N at 403 in Figure 4.10 (b). Graphitic nitrogen typically refers to nitrogen atoms that occupy positions within the graphitic lattice, often associated with substitutional doping where nitrogen

replaces carbon atoms in the hexagonal carbon network. This form of nitrogen is thought to contribute to the material's electrical characteristics via increasing conductivity and modifying chemical reactivity (Figueras et al., 2019).

Table 4.2

The characterization of AC700

Sample	Specific surface area (m ² g ⁻¹)	Pore volume (cm ³ g ⁻¹)	Pore diameter (nm)	Atomic concentration (%)			
				C	O	N	S
AC700-1	1141	0.16	1.78	87.09	11.24	0.90	-
AC700-2	1663	0.33	1.91	87.87	10.34	1.24	0.17
AC700-3	1334	0.43	1.71	84.42	12.57	1.45	0.45

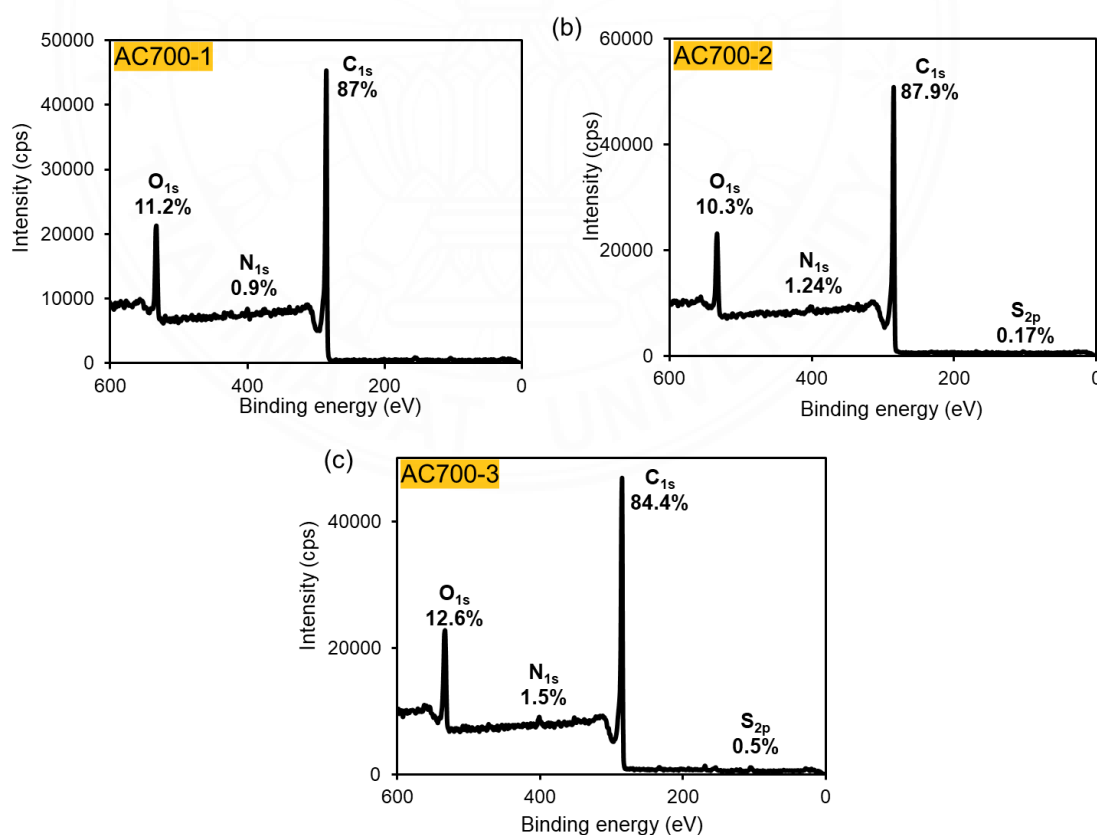


Figure 4.8 The survey XPS spectrum of AC700 (a) AC700-1, (b) AC700-2, and (c) AC700-3

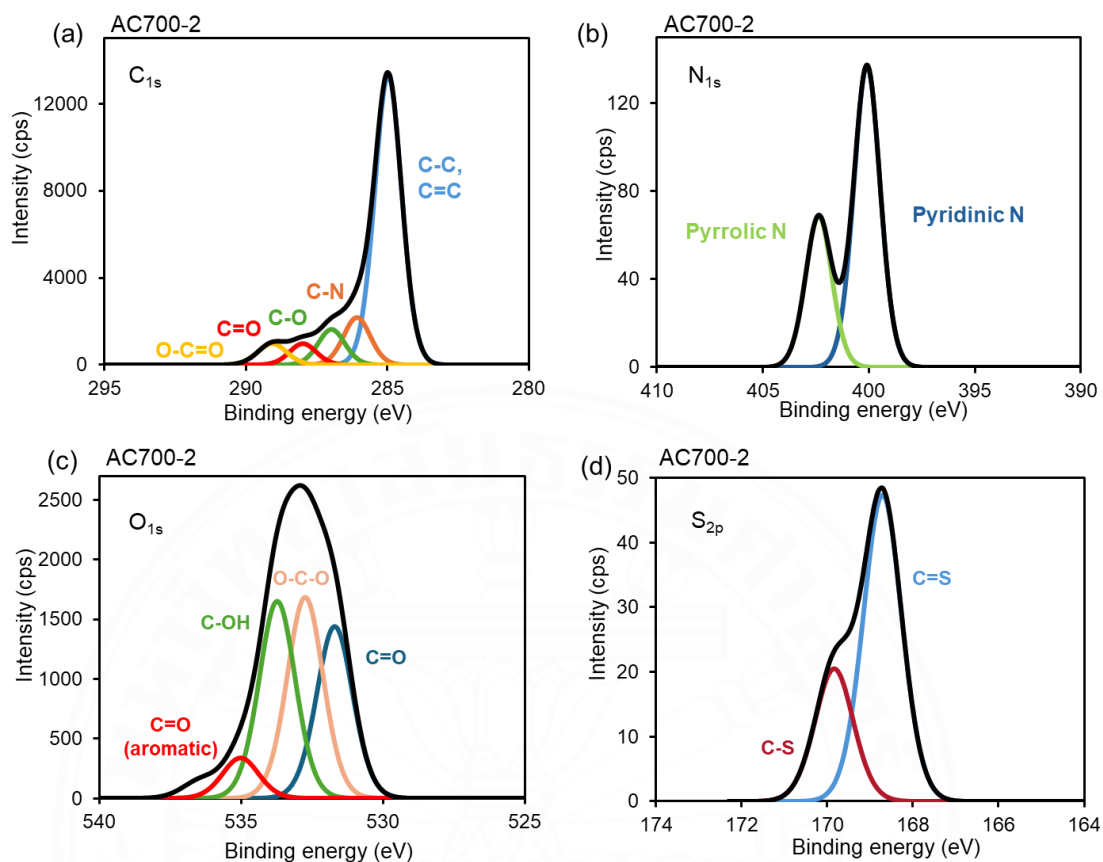


Figure 4.9 (a) high-resolution spectra of C_{1s} , (b) high-resolution spectra of N_{1s} , (c) high-resolution spectra of O_{1s} , and (d) high-resolution spectra of S_{2p} of AC700-2

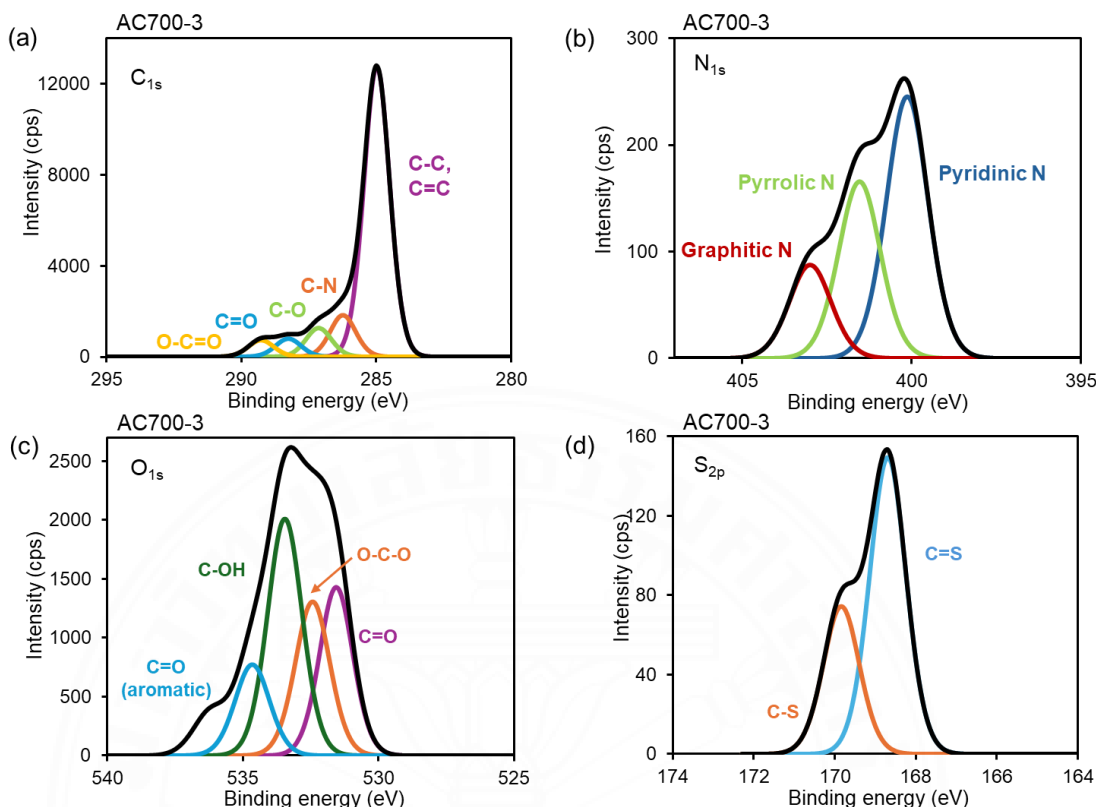


Figure 4.10 (a) high-resolution spectra of C_{1s} , (b) high-resolution spectra of N_{1s} , (c) high-resolution spectra of O_{1s} , and (d) high-resolution spectra of S_{2p} of AC700-3

4.3 Electrochemical performance of AC800

The CV was used to examine the electrochemical characterization of hemp core-derived activated carbon. The cyclic voltammograms were obtained for a comparison of the types of electrodes using a standard 3 M KOH solution as the electrolyte. Figure 4.11 (a) illustrated that AC800-1 displayed the largest area under the curve, resulting in the highest specific capacitance recorded at 175 F g^{-1} at scan rate of 30 mV s^{-1} within a potential range of -0.8 to 0.2 V . This is due to its high surface area, but the dopant doesn't enhance performance due to the extreme activation conditions.

Nonetheless, CV curves in Figure 4.11 (b) show the performance of the AC800-1 electrode which exhibits an escalating current trend with rising scan rates up

to 100 mV s^{-1} . This pattern indicates the diffusion of electrolyte ions, signifying low internal resistance and expedited kinetics. Additionally, the electrode's distinctive quasi-rectangular shape signifies characteristics ideal EDLC.

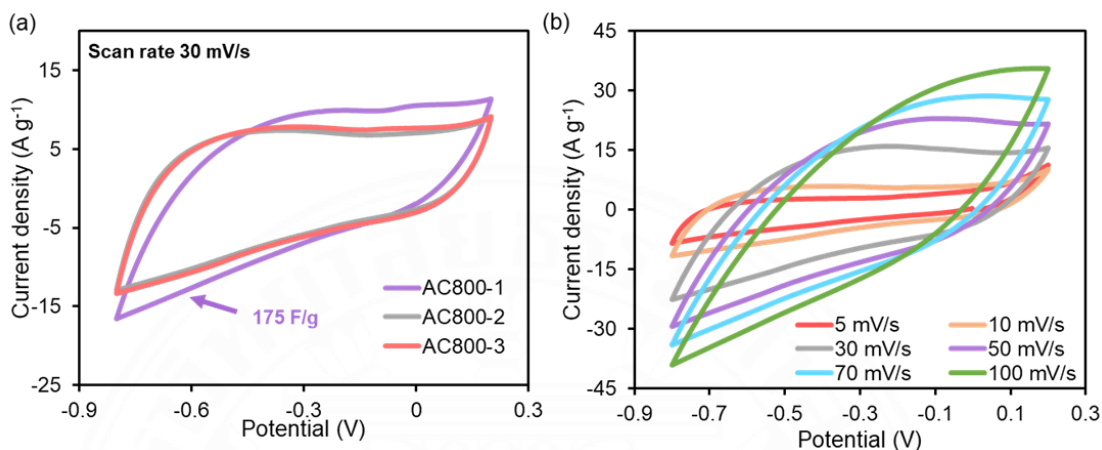


Figure 4.11 (a) CV curves comparison of various electrode at scan rate 30 mV s^{-1} , and (b) CV curves of AC800-1 electrode at different scan rates ($5, 10, 30, 50, 70$ and 100 mV s^{-1})

4.4 Electrochemical performance of AC700

The activated carbon derived from hemp cores was used as an electrode material. Pyroligneous acid, a byproduct of hemp char production, was utilized as an electrolyte solution and compared with the aqueous KOH electrolyte for the construction of supercapacitors. A potentiostat/galvanostat was employed to evaluate the electrochemical properties of activated carbon derived from hemp core. Cyclic voltammograms were recorded to compare electrode performance, utilizing a standard 3M KOH solution as the electrolyte. Among the samples, AC700-2 demonstrated the highest specific capacitance of 510 F g^{-1} at a scan rate of 30 mV s^{-1} within a potential range of -1 to 0 V shows in Figure 4.12 (a). This observation underscores that the introduction of heteroatoms into the activated carbon structure significantly enhances its electrochemical performance. This improvement can be attributed to an enhancement in specific surface area and morphology, leading to increased wettability.

The refined morphology contributes to the presence of highly active sites within the structure (Dujearic-Stephane et al., 2021; Thillaikkarasi et al., 2022).

Galvanostatic charge/discharge measurements conducted at a current density of 2.5 A g^{-1} revealed that AC700-2 exhibited superior stability and capacitance. This performance highlights the presence of micropores and mesopores in the activated carbon samples, with the EDLC curve displaying (Figure 4.12 (b)) an ideal symmetric shape (Chen et al., 2018).

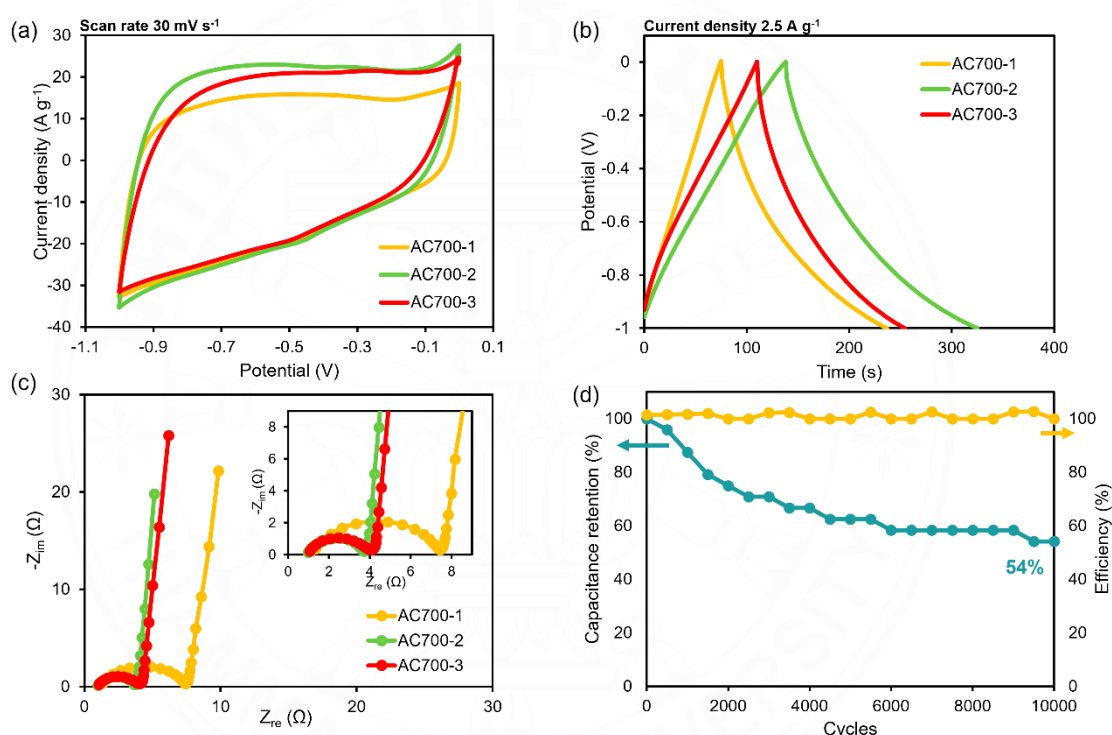


Figure 4.12 (a) CV curves of AC electrode in 3M KOH electrolyte at a scan rate of 30 mV s^{-1} , (b) GCD curves of AC electrode in 3M KOH electrolyte at current density of 2.5 A g^{-1} , (c) EIS spectra of AC electrode in 3M KOH electrolyte, and (d) capacitance retention of AC700-2 in 3M KOH electrolyte

The EIS spectra revealed a semicircle corresponding to the overall resistance (R_s) and the charge transfer resistance (R_{ct}) as shown in the Nyquist plot (Figure 4.12 (c)). The R_s accounts for the resistance of the electrolyte, the carbon material, and the contact interfaces. AC700-2 and AC700-3 demonstrated lower R_{ct}

values (2.73 Ω and 3.08 Ω , respectively) than AC700-1 (6.29 Ω), which can be attributed to the incorporation of nitrogen and sulfur heteroatoms into the carbon structure. This doping effectively enhances the material's conductivity and boosts its electrochemical performance. Moreover, figure 4.12 (d) the system of AC700-2 in 3M KOH standard electrolyte shows a capacitance retention of 54% after 10,000 cycles with high efficiency.

The results indicate that incorporating N and S into the structure enhances its pseudocapacitive properties, significantly improving its efficiency. The additional pseudocapacitive behavior arises from reversible redox reactions occurring at the electrode-electrolyte interface. A possible reaction mechanism is illustrated in Figure 4.13 (Dubey et al., 2023).

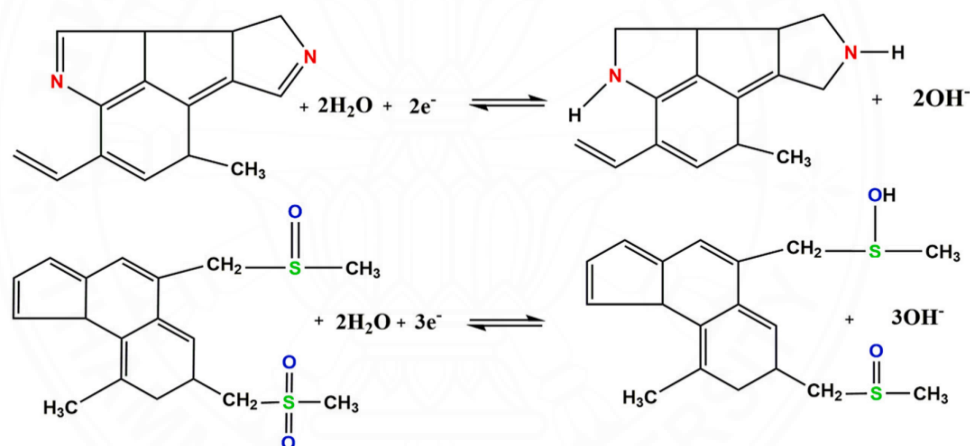


Figure 4.13 Probable reversible redox reactions due to N, S doping. Adapted from “Effect of nitrogen and sulfur co-doping on the surface and diffusion characteristics of date seed-derived porous carbon for asymmetric supercapacitors”, Journal of Energy Storage. (Dubey et al., 2023)

4.5 Electrochemical properties of Pyroligneous acid electrolytes

The electrolyte was fabricated from 3M KOH compared with KOH/PA electrolyte and used AC700-2 as an electrode. The KOH/PA became basicity for less

corrosion for improve the performance. As shown in Figure 4.14 (a), the CV from AC700-2 in 3M KOH/PA was larger than other electrolytes show the result of specific capacitance of 672 F g^{-1} at 30 mV s^{-1} , which is equivalent to a 131.76% increase. As a consequence, 3M KOH/PA electrolyte is a potential alternative aqueous electrolyte because it has higher electrical performance, is less expensive than KOH, and provides the most valuable use of biological waste.

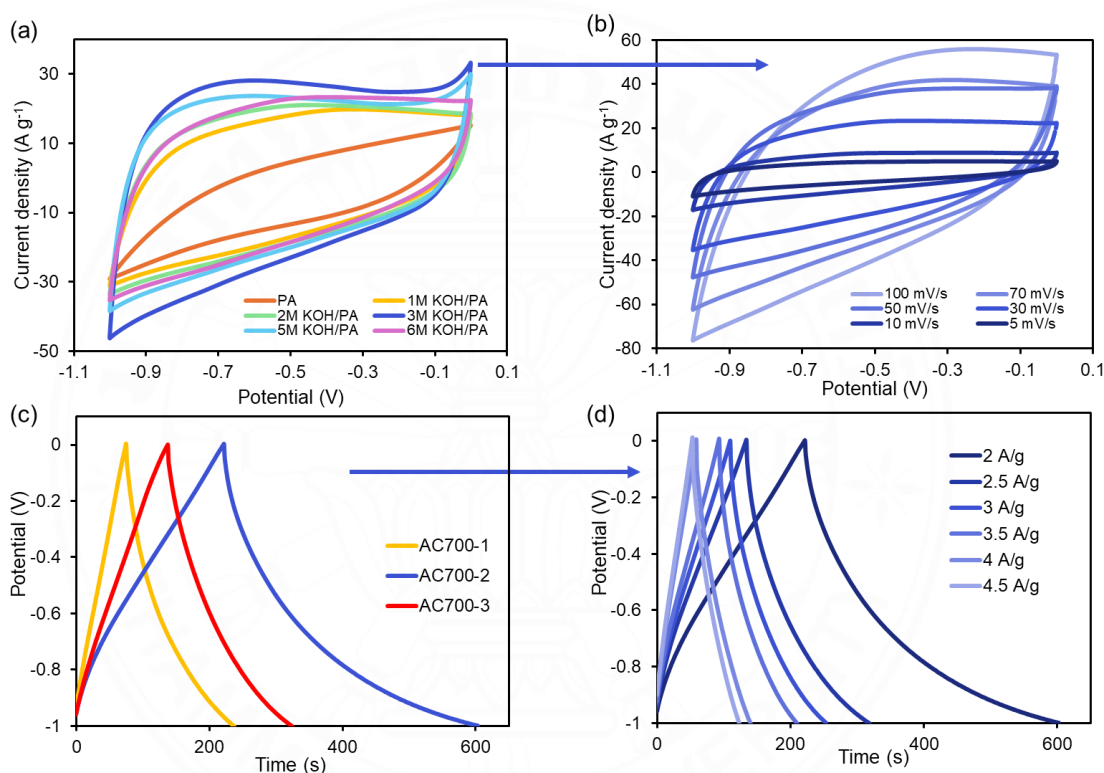


Figure 4.14 (a) CV curves of mixing various concentrations of KOH in PA, (b) CV curves of AC700-2 electrode in 3M KOH/PA electrolyte at different scan rates (5, 10, 30, 50, 70 and 100 mV s^{-1}), (c) GCD curve of all types of AC in 3M KOH/PA, and (d) GCD curve of AC700-2 electrode in 3M KOH/PA electrolyte at different current densities (2, 2.5, 3, 3.5, 4 and 4.5 A g^{-1})

The working electrode AC700-2 provides a higher current with increasing scan rates up to 100 mV s^{-1} , revealing the simplicity of availability of electrolyte ions,

low internal resistance, enhanced rate capability, and faster kinetics for EDLC formation and show the large surface area and pore distribution of the working electrode AC700-2 (Raj et al., 2022), as shown in figure 4.14 (b). A detailed inspection also reveals the characteristic quasi rectangular box shape ideal for EDLC.

GCD curves all types of AC in 3M KOH/PA in figure 4.14 (c) was used to confirm the electrochemical performance of the system shown that AC700-2 indicates the highest potential. Moreover, GCD curves of working electrode AC700-2 are perfectly triangular leads to EDLC behavior. Furthermore, at different current densities, a modest IR drop reflects the electron transfer resistance in the active materials as well as the ion diffusion resistance in the electrolyte, demonstrating ideal capacitive behavior as demonstrated in Figure 4.14 (d).

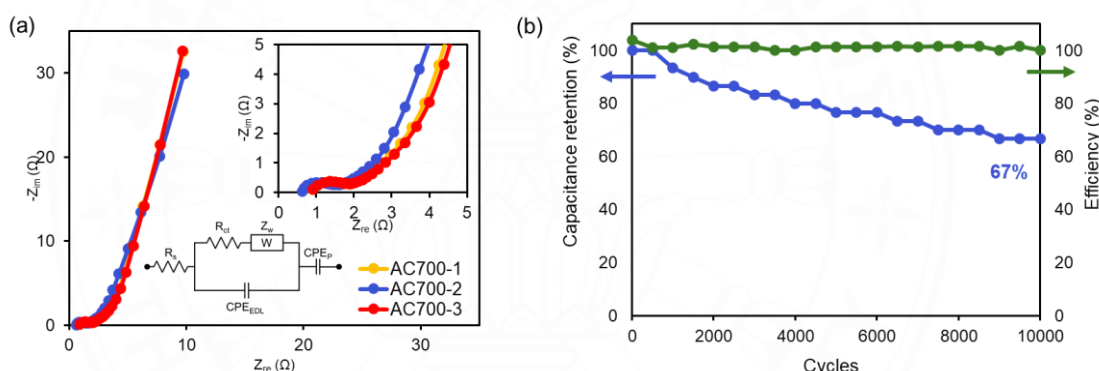


Figure 4.15 (a) EIS spectra of AC electrode in 3M KOH/PA electrolyte, and (b) capacitance retention of AC700-2 in 3M KOH/PA electrolyte

The EIS spectra of all AC electrode in 3M KOH/PA electrolyte demonstrate reduced overall resistance (R_s) and the charge transfer resistance (R_{ct}) compared to standard electrolyte and AC700-2 indicates the lowest R_s (0.6Ω) and R_{ct} (0.9Ω), highlighting its superior performance. The EIS plots can be fitted to the equivalent circuit in Figure 4.15 (a), where R_s , CPE_{EDL} , R_{ct} , Z_w and CPE_P are internal resistance, the EDLC, the charge transfer resistance, the diffusion resistance and the pseudocapacitance, respectively.

A two-electrode symmetric capacitor was assembled with AC700-2 electrode in 3M KOH/PA electrolyte, the best-performing electrode in the study. After

10,000 cycles, the capacitance retention of the as-prepared symmetric capacitor was 67%, which is 13% higher from previous conditions, suggesting excellent long-term cycling stability (Figure 4.15 (b)). These findings demonstrate that N and S co-doped carbon derived from hemp core is a good material for applications in energy conversion and storage devices. The electrochemical results revealed that AC700-2 material is viable as a high-performance supercapacitor electrode.

4.6 Analysis of capacitance contribution

The analysis of capacitance contribution in supercapacitors is a critical aspect of understanding their performance and capacitive behaviors. The charge storage and ion transport of AC700 with different amounts of thiourea dopant in 3M KOH standard electrolyte were investigated under different scan rate 5-100 mV s⁻¹ using Dunn's method. Experimental results reveal that increasing the N and S content in the material enhances its diffusion-controlled contribution, which becomes more significant at lower scan rates. The research demonstrates that a decrease in scan rate results in a greater influence of diffusion-controlled processes as shown in Figure 4.16. This occurs because lower scan rates provide sufficient time for ions to diffuse to the electrode surface, promoting charge transfer and increasing the diffusion-dominated current response (Masood, Muhammad, & Tahiri, 2024). In contrast, at higher scan rates, the limited time for ion diffusion shifts the dominant mechanism to capacitive contributions, where charge accumulation occurs primarily at the interface without extensive ion movement. At slower scan rates, ions can effectively penetrate the porous structure of the electrode material, thereby boosting diffusion-driven charge storage mechanisms (Kim et al., 2020).

In contrast, AC700 in 3M KOH/PA electrolyte predominantly exhibits a surface-controlled contribution in Figure 4.17. This behavior is attributed to the chemical composition of pyroligneous acid, which primarily comprises large organic molecules. As a result, ion exchange between the electrode and electrolyte primarily occurs at the surface, rather than within the diffusion-controlled contribution. Surface-controlled mechanisms, often characterized by capacitive effects, enable much faster charge and discharge rates compared to diffusion-controlled processes. This rapid

kinetics is essential for applications requiring quick energy delivery, which enhances electrochemical performance (Park, 2024; J. Wang et al., 2016). The surface-controlled contribution aligns with the observed higher capacitance retention in the 3M KOH/PA electrolyte. This is due to reduced ion mass transport compared to diffusion-controlled mechanisms, which minimizes energy losses from resistive heating and other inefficiencies during operation. This contributes to the overall efficiency of the supercapacitor system (Park, 2024).

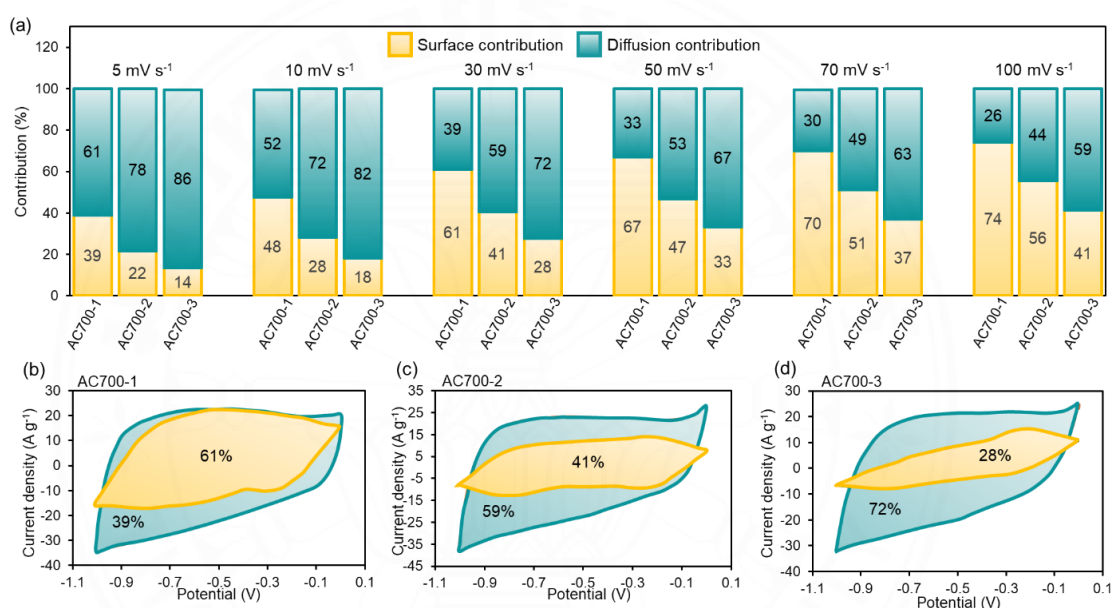


Figure 4.16 (a) Ratio between surface contribution and diffusion contribution of AC700 electrode in 3M KOH electrolyte, (b) Ratio of AC700-1 at scan rate 30 mV s⁻¹, (c) Ratio of AC700-2 at scan rate 30 mV s⁻¹, and (d) Ratio of AC700-3 at scan rate 30 mV s⁻¹

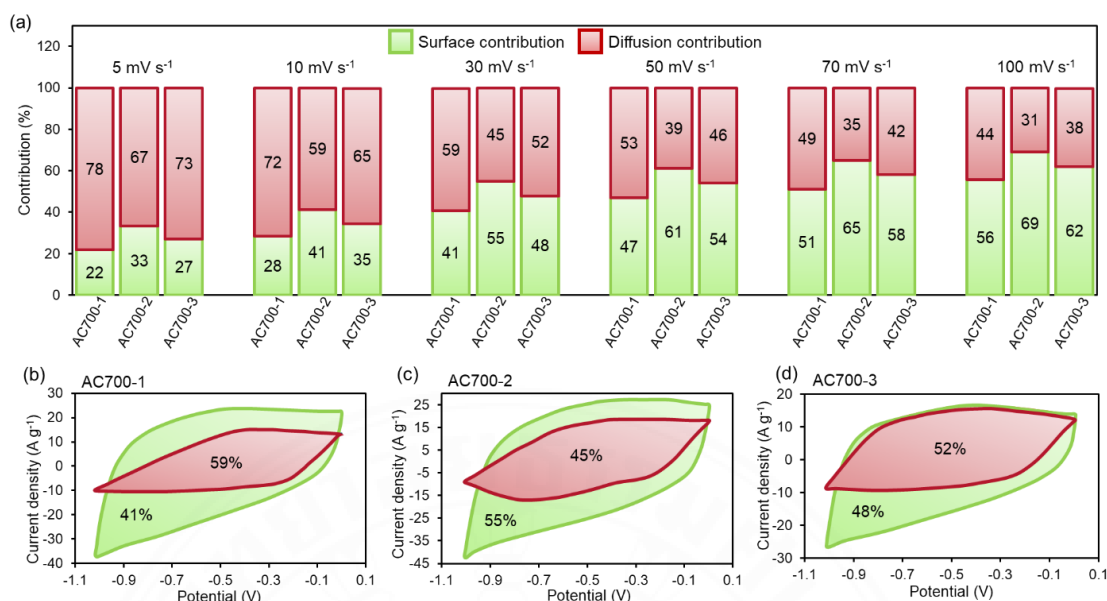


Figure 4.17 (a) Ratio between surface contribution and diffusion contribution of AC700 electrode in 3M KOH/PA electrolyte, (b) Ratio of AC700-1 at scan rate 30 mV s⁻¹, (c) Ratio of AC700-2 at scan rate 30 mV s⁻¹, and (d) Ratio of AC700-3 at scan rate 30 mV s⁻¹

4.7 Contact angle measurement

The introduction of N and S into the activated carbon structure alters the surface chemistry of the activated carbon. Nitrogen introduces pyridinic and pyrrolic groups, while sulfur contributes thiol and sulfonic groups. These functional groups can significantly affect the wettability of the surface (Uppugalla et al., 2023). Studies have demonstrated that N, S-doping reduces the contact angle of activated carbon surfaces, reflecting improved hydrophilicity. As shown in Figure 4.18, the same electrolyte exhibits lower contact angles when the thiourea content is increased. The relationship between contact angle and specific capacitance highlights the significant link between supercapacitor performance and the hydrophilicity of the electrode (Jorn-am et al., 2023). Moreover, the adding of pyroligneous acid in electrolyte can improve the wettability in Fig 4.18 shows that after two seconds droplet of 3M KOH/PA completely absorb into AC700-2 and AC700-3 electrodes. A hydrophilic surface facilitates the penetration of the electrolyte into the inner material, leading to a higher specific

capacitance. This enhances the interaction between the electrode and electrolyte, as well as ion adsorption and diffusion.

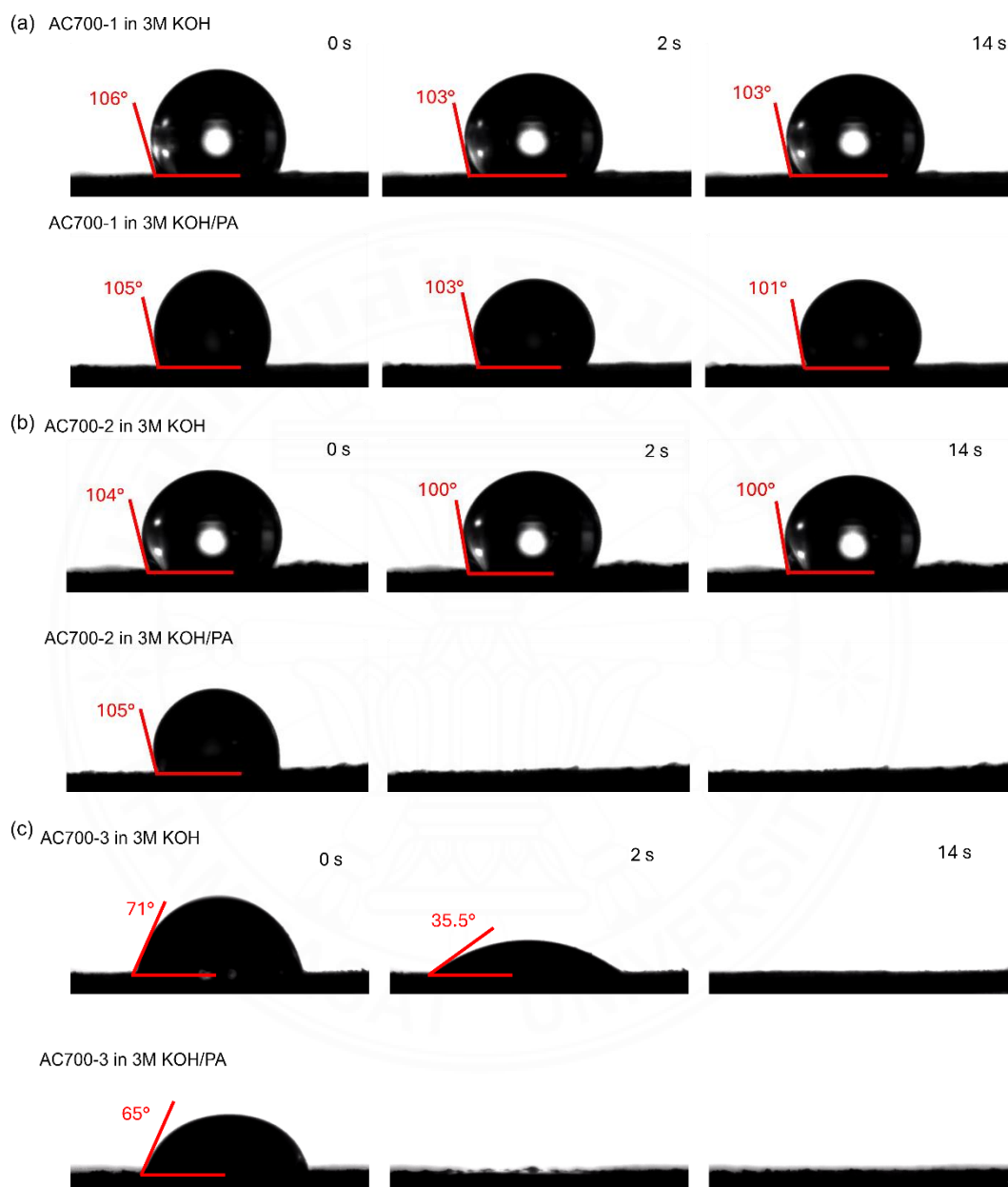


Figure 4.18 Contact angle of AC700 electrode in 3M KOH electrolyte compared to 3M KOH/PA electrolyte

CHAPTER 5

CONCLUSIONS AND RECOMMENDATIONS

5.1 Conclusions

The symmetric supercapacitor was fabricated using hemp core-derived activated carbon as an active material and improved the performance using thiourea as a nitrogen (N) and sulfur (S) source for heteroatom doping. In this research, the study focused on the factors influencing the synthesis of activated carbon by comparing the amounts of thiourea doped at 10% wt and 20% wt. Additionally, it compared activation temperatures of 800°C with a heat rate of 10°C/minute (AC800) against 700°C with a heat rate of 5°C/minute (AC700). The findings indicated that the factors affecting the enhancement of supercapacitor performance depend on several variables, such as surface area and the content of N and S elements. This is because the incorporation of heteroatom doping plays a crucial role in improving electrochemical properties; S-doped activated carbon can undergo reversible redox reactions with electrolyte ions, forming sulfide and thiol groups (Shaheen Shah, Abu Nayem, Sultana, Saleh Ahammad, & Abdul Aziz, 2022). Furthermore, nitrogen introduces pyridinic and pyrrolic groups, which improve the wettability of the surface.

At a temperature of 800°C, doping with thiourea increased the specific surface area by 1.2 times, from 1547 m² g⁻¹ to 1853 m² g⁻¹. However, extreme doping conditions resulted in the absence of N and S elements in the structure of activated carbon, leading to poor supercapacitor performance. This was evidenced by the specific capacitance of undoped activated carbon (AC800-1), which was only 175 F g⁻¹. In contrast, when the doping temperature was set at 700°C, the activation process became more effective. As a result, thiourea doping increased the specific surface area by 1.46 times, from 1141 m² g⁻¹ to 1663 m² g⁻¹, and incorporated N and S elements into the structure of activated carbon.

As a result, the 20%wt thiourea-doped activated carbon (AC700-2) possesses a specific capacitance of 510 F g⁻¹ (scan rate 30 mV s⁻¹). Furthermore, to make optimal use of biological waste, pyrroligneous acid, a byproduct of hemp charcoal

production, is utilized as an electrolyte. As a result, the fabricated supercapacitor exhibits a specific capacitance reaching up to 672 F g^{-1} , which is 1.32 times higher than the controlled electrolyte and 3.84 times greater than the previous condition. Additionally, the fabrication of N, S activated carbon in 3M KOH/PA electrolyte supercapacitor exhibits high energy density of 106 Wh kg^{-1} at a power density of 999.9 W kg^{-1} . In conclusion, the doping of nitrogen and sulfur into activated carbon exhibited enhanced surface area, porosity, wettability, and electrochemical performance this research presents an innovative approach leveraging renewable biomass sources to create high-performance supercapacitors, emphasizing improved functionality and practical application prospects. The findings underscore the importance of utilizing agricultural waste in producing sustainable materials for energy storage. The dual doping strategy not only enhances the surface area and porosity but also improves the electrochemical performance metrics, including energy density and power density. This work contributes to the growing of knowledge on sustainable energy solutions and highlights the viability of using biowaste to create effective supercapacitor materials.

5.2 Recommendations

5.2.1 Investigation of Alternative Biomass Sources: Future research should explore various biomass materials beyond hemp, such as agricultural residues or forestry byproducts, to assess their potential for producing activated carbon with superior electrochemical properties. This could help identify other sustainable sources for high-performance supercapacitors.

5.2.2 Integration with Renewable Energy Systems: Future work should investigate the integration of these supercapacitors with renewable energy sources, such as solar or wind power systems, to evaluate their performance in hybrid energy setups and their capacity to stabilize intermittent energy generation.

5.2.3 Advanced Characterization Techniques: Employing advanced characterization methods, such as in situ spectroscopy or high-resolution electron microscopy, could provide deeper insights into the structural changes occurring during charge/discharge cycles. Understanding these mechanisms will be critical for optimizing material design for enhanced performance.

REFERENCES

- Adeleye, A. T., Akande, A. A., Odoh, C. K., Philip, M., Fidelis, T. T., Amos, P. I., & Banjoko, O. O. (2021). Efficient synthesis of bio-based activated carbon (AC) for catalytic systems: A green and sustainable approach. *Journal of Industrial and Engineering Chemistry*, 96, 59-75.
- Azmi, N. Z. M., Buthiyappan, A., Raman, A. A. A., Patah, M. F. A., & Sufian, S. (2022). Recent advances in biomass based activated carbon for carbon dioxide capture—A review. *Journal of Industrial and Engineering Chemistry*, 116, 1-20.
- Castro-Gutiérrez, J., Celzard, A., & Fierro, V. (2020). Energy storage in supercapacitors: Focus on tannin-derived carbon electrodes. *Frontiers in materials*, 7, 217.
- Chen, H., Yu, F., Wang, G., Chen, L., Dai, B., & Peng, S. (2018). Nitrogen and sulfur self-doped activated carbon directly derived from elm flower for high-performance supercapacitors. *ACS omega*, 3(4), 4724-4732.
- Childres, I., Jauregui, L. A., Park, W., Cao, H., & Chen, Y. P. (2013). Raman spectroscopy of graphene and related materials. *New developments in photon and materials research*, 1, 1-20.
- Conway, B. E., Birss, V., & Wojtowicz, J. (1997). The role and utilization of pseudocapacitance for energy storage by supercapacitors. *Journal of Power Sources*, 66(1), 1-14. doi:[https://doi.org/10.1016/S0378-7753\(96\)02474-3](https://doi.org/10.1016/S0378-7753(96)02474-3)
- Dai, Z., Ren, P.-G., Guo, Z., He, W., Hou, X., & Jin, Y. (2021). Three-dimensional porous carbon materials derived from locust for efficient NOS co-doped supercapacitors by facile self-template and in-situ doping method. *Fuel Processing Technology*, 213, 106677.
- Deitch, R. (2003). *Hemp: American history revisited: the plant with a divided history*: Algora Publishing.
- Dubey, P., Maheshwari, P. H., Shrivastav, V., & Sundriyal, S. (2023). Effect of nitrogen and sulphur co-doping on the surface and diffusion characteristics of date seed-derived porous carbon for asymmetric supercapacitors. *Journal of Energy Storage*, 58, 106441.

- Dujearic-Stephane, K., Gupta, M., Kumar, A., Sharma, V., Pandit, S., Bocchetta, P., & Kumar, Y. (2021). The effect of modifications of activated carbon materials on the capacitive performance: surface, microstructure, and wettability. *Journal of Composites Science*, 5(3), 66.
- Erickson, B. (2019). USDA releases hemp production requirements. *C&EN Global Enterp*, 97(43), 17.
- Figueras, M., Villar-Garcia, I. J., Vines, F., Sousa, C., de la Peña O'Shea, V. A., & Illas, F. (2019). Correcting flaws in the assignment of nitrogen chemical environments in N-doped graphene. *The Journal of Physical Chemistry C*, 123(17), 11319-11327.
- Gandolfi, S., Ottolina, G., Riva, S., Fantoni, G. P., & Patel, I. (2013). Complete Chemical Analysis of Carmagnola Hemp Hurds and Structural Features of Its Components. *BioResources*(8(2)).
- Grewal, A., Abbey, L., & Gunupuru, L. R. (2018). Production, prospects and potential application of pyrolygneous acid in agriculture. *Journal of analytical and applied pyrolysis*, 135, 152-159.
- Hartsel, J. A., Eades, J., Hickory, B., & Makriyannis, A. (2016). Chapter 53 - Cannabis sativa and Hemp. In R. C. Gupta (Ed.), *Nutraceuticals* (pp. 735-754). Boston: Academic Press.
- Heidarinejad, Z., Dehghani, M. H., Heidari, M., Javedan, G., Ali, I., & Sillanpää, M. (2020). Methods for preparation and activation of activated carbon: a review. *Environmental Chemistry Letters*, 18(2), 393-415. doi:10.1007/s10311-019-00955-0
- Hsu, C.-C., Tu, Y.-H., Yang, Y.-H., Wang, J.-A., & Hu, C.-C. (2020). Improved performance and long-term stability of activated carbon doped with nitrogen for capacitive deionization. *Desalination*, 481, 114362.
- Hu, L., Zeng, F., Song, X., Liang, J., Zhang, X., Zhou, H., . . . Jiang, C. (2023). Synthesis, analysis and characterization of nitrogen/sulfur co-doped activated carbon for high-performance all-printed flexible supercapacitor. *Journal of Energy Storage*, 73, 109004.

- Ibrahim, H., Ilinca, A., & Perron, J. (2008). Energy storage systems—Characteristics and comparisons. *Renewable and Sustainable Energy Reviews*, 12(5), 1221-1250. doi:<https://doi.org/10.1016/j.rser.2007.01.023>
- Jahanban-Esfahlan, A., & Amarowicz, R. (2018). Walnut (*Juglans regia* L.) shell pyrolygneous acid: chemical constituents and functional applications. *RSC advances*, 8(40), 22376-22391.
- Ji, L., Wang, B., Yu, Y., Wang, N., & Zhao, J. (2020). N, S co-doped biomass derived carbon with sheet-like microstructures for supercapacitors. *Electrochimica Acta*, 331, 135348.
- Jorn-am, T., Pholauyphon, W., Supchocksoonthorn, P., Sirisit, N., Chanthad, C., Manyam, J., . . . Paoprasert, P. (2023). High-performance supercapacitors using synergistic hierarchical Ni-doped copper compounds/activated carbon composites with MXenes and carbon dots as simultaneous performance enhancers. *Electrochimica Acta*, 447, 142147.
- Kazempour, S. J., Moghaddam, M. P., Haghifam, M. R., & Yousefi, G. R. (2009). Electric energy storage systems in a market-based economy: Comparison of emerging and traditional technologies. *Renewable Energy*, 34(12), 2630-2639. doi:<https://doi.org/10.1016/j.renene.2009.04.027>
- Keçili, R., Arli, G., & Hussain, C. M. (2020). Future of analytical chemistry with graphene. In *Comprehensive Analytical Chemistry* (Vol. 91, pp. 355-389): Elsevier.
- Keller, N. M. (2013). The legalization of industrial hemp and what it could mean for Indiana's biofuel industry. *Ind. Int'l & Comp. L. Rev.*, 23, 555.
- Khlangsap, N., Tara, A., & Jamornchotisn, P. (2011). How to make pyrolygneous acid. *Kasetsart University*, 54(2), 1-13.
- Kim, T., Choi, W., Shin, H.-C., Choi, J.-Y., Kim, J. M., Park, M.-S., & Yoon, W.-S. (2020). Applications of voltammetry in lithium ion battery research. *Journal of Electrochemical Science and Technology*, 11(1), 14-25.
- Koohi-Fayegh, S., & Rosen, M. A. (2020). A review of energy storage types, applications and recent developments. *Journal of Energy Storage*, 27, 101047. doi:<https://doi.org/10.1016/j.est.2019.101047>

- Lee, J. Y., Kim, N. Y., Shin, D. Y., Park, H.-Y., Lee, S.-S., Joon Kwon, S., . . . Kim, J. Y. (2017). Nitrogen-doped graphene-wrapped iron nanofragments for high-performance oxygen reduction electrocatalysts. *Journal of Nanoparticle Research*, 19(3), 98.
- Li, Y., Tian, C., Zhang, N., Zhao, A., Bai, X., Yi, W., & Fu, P. (2021). Hydrothermal Liquefaction of Cornstalk by Reusing Pyroligneous Acid: Synergistic Effects on Biocrude Oil Formation and Solid Residue Accumulation. *Energy & Fuels*, 36(1), 435-449.
- Libich, J., Máca, J., Vondrák, J., Čech, O., & Sedlaříková, M. (2018). Supercapacitors: Properties and applications. *Journal of Energy Storage*, 17, 224-227. doi:<https://doi.org/10.1016/j.est.2018.03.012>
- Lin, Y., Huang, C., Huang, C., Deng, Y., Zou, X., Ma, W., . . . Ragauskas, A. J. (2024). Cellulose regulated lignin/cellulose-based carbon materials with hierarchical porous structure for energy storage. *Advanced Composites and Hybrid Materials*, 7(2), 51.
- Liu, F., Niu, J., Chuan, X., & Zhao, Y. (2023). Effect of carbonization atmosphere on electrochemical properties of nitrogen-doped porous carbon. *Frontiers of Materials Science*, 17(4), 230669. doi:10.1007/s11706-023-0669-1
- Liu, J., Wang, J., Xu, C., Jiang, H., Li, C., Zhang, L., . . . Shen, Z. X. (2018). Advanced Energy Storage Devices: Basic Principles, Analytical Methods, and Rational Materials Design. *Adv Sci (Weinh)*, 5(1), 1700322. doi:10.1002/advs.201700322
- Liu, Y., Wu, Q., Liu, L., Manasa, P., Kang, L., & Ran, F. (2020). Vanadium nitride for aqueous supercapacitors: a topic review. *Journal of materials chemistry A*, 8(17), 8218-8233.
- Ma, Y. (2017). Comparison of activated carbons prepared from wheat straw via ZnCl₂ and KOH activation. *Waste and biomass valorization*, 8, 549-559.
- Malini, K., Selvakumar, D., & Kumar, N. (2023). Activated carbon from biomass: Preparation, factors improving basicity and surface properties for enhanced CO₂ capture capacity—A review. *Journal of CO₂ Utilization*, 67, 102318.

- Masood, Z., Muhammad, H., & Tahiri, I. A. (2024). Comparison of Different Electrochemical Methodologies for Electrode Reactions: A Case Study of Paracetamol. *Electrochem*, 5(1), 57-69.
- Mathew, S., & Zakaria, Z. A. (2015). Pyroligneous acid—the smoky acidic liquid from plant biomass. *Applied microbiology and biotechnology*, 99, 611-622.
- McLean, Virginia, A., Halper, M. S., & Ellenbogen, J. C. (2006). *Supercapacitors : A Brief Overview*.
- Muthuraj, D., Ghosh, A., Kumar, A., & Mitra, S. (2019). Nitrogen and sulfur doped carbon cloth as current collector and polysulfide immobilizer for magnesium-sulfur batteries. *ChemElectroChem*, 6(3), 684-689.
- Nasser, R., Tiantian, J., & Song, J.-M. (2022). Hierarchical porous activated carbon derived from olives: Preparation, (N, S) co-doping, and its application in supercapacitors. *Journal of Energy Storage*, 51, 104348.
- Olabi, A. G. (2017). Renewable energy and energy storage systems. *Energy*, 136, 1-6. doi:<https://doi.org/10.1016/j.energy.2017.07.054>
- Park, B.-N. (2024). Differential Analysis of Surface-Dominated vs. Bulk-Dominated Electrochemical Processes in Lithium Iron Phosphate Cathodes. *Korean Journal of Metals and Materials*, 62(8), 624-630.
- Raj, F. R. M. S., Boopathi, G., Kalpana, D., Jaya, N. V., & Pandurangan, A. (2022). Sustainable development through restoration of *Prosopis juliflora* species into activated carbon as electrode material for supercapacitors. *Diamond and Related Materials*, 121, 108767.
- Raj, F. R. M. S., Jaya, N. V., Boopathi, G., Kalpana, D., & Pandurangan, A. (2020). S-doped activated mesoporous carbon derived from the *Borassus flabellifer* flower as active electrodes for supercapacitors. *Materials Chemistry and Physics*, 240, 122151.
- Shaheen Shah, S., Abu Nayem, S., Sultana, N., Saleh Ahammad, A., & Abdul Aziz, M. (2022). Preparation of sulfur-doped carbon for supercapacitor applications: a review. *ChemSusChem*, 15(1), e202101282.
- Shao, Y., El-Kady, M. F., Sun, J., Li, Y., Zhang, Q., Zhu, M., . . . Kaner, R. B. (2018). Design and Mechanisms of Asymmetric Supercapacitors. *Chemical Reviews*, 118(18), 9233-9280. doi:10.1021/acs.chemrev.8b00252

- Sharma, P., & Kumar, V. (2020). Study of electrode and electrolyte material of supercapacitor. *Materials today: proceedings*, 33, 1573-1578.
- Shukla, A. K., Sampath, S., & Vijayamohanan, K. (2000). Electrochemical supercapacitors: Energy storage beyond batteries. *Current Science*, 79(12), 1656-1661. Retrieved from <http://www.jstor.org/stable/24104124>
- Singh, G., Kim, I. Y., Lakhi, K. S., Joseph, S., Srivastava, P., Naidu, R., & Vinu, A. (2017). Heteroatom functionalized activated porous biocarbons and their excellent performance for CO₂ capture at high pressure. *Journal of materials chemistry A*, 5(40), 21196-21204.
- Sultana, M., Rownok, M. H., Sabrin, M., Rahaman, M. H., & Alam, S. N. (2022). A review on experimental chemically modified activated carbon to enhance dye and heavy metals adsorption. *Cleaner engineering and technology*, 6, 100382.
- Süzerer, V., Tilkat, E., Onay, A., & Fidan, M. (2023). INDUSTRIAL HEMP SEED: PRODUCTION, CHEMICAL CONTENT AND POTENTIAL USES FOR HUMAN NUTRITION. *Türk Bilimsel Derlemeler Dergisi*, 16(1), 29-53.
- Thillaikkarasi, D., Karthikeyan, S., Ramesh, R., Sengodan, P., Kavitha, D., & Muthubalasubramanian, M. (2022). Electrochemical performance of various activated carbon-multi-walled carbon nanotubes symmetric supercapacitor electrodes in aqueous electrolytes. *Carbon Letters*, 32(6), 1481-1505.
- Thomsen, A. B., Rasmussen, S. K., Bohn, V., Nielsen, K. V., & Thygesen, A. (2005). Hemp raw materials: The effect of cultivar, growth conditions and pretreatment on the chemical composition of the fibres. (Risoe-R No. 1507(EN)).
- Thumkaew, Y., Praneerad, J., Manyam, J., Chanthad, C., Liang, X., Song, S., . . . Paoprasert, P. (2022). High-Performance Supercapacitors Fabricated from Sugarcane Waste-derived Activated Carbon Electrodes and Carbon Dot-added Molasses as Electrolytes. *ChemistrySelect*, 7(28), e202202051.
- Tourangeau, W. (2015). Re-defining environmental harms: Green criminology and the state of Canada's hemp industry. *Canadian Journal of Criminology and Criminal Justice*, 57(4), 528-554.
- Uppugalla, S., Pothu, R., Boddula, R., Desai, M. A., & Al-Qahtani, N. (2023). Nitrogen and sulfur co-doped activated carbon nanosheets for high-performance coin cell

- supercapacitor device with outstanding cycle stability. *Emergent Materials*, 6(4), 1167-1176.
- Vangari, M., Pryor, T., & Jiang, L. (2013). Supercapacitors: Review of Materials and Fabrication Methods. *Journal of Energy Engineering*, 139(2), 72-79. doi:10.1061/(ASCE)EY.1943-7897.0000102
- Wang, C., Zhou, E., He, W., Deng, X., Huang, J., Ding, M., . . . Xu, X. (2017). NiCo₂O₄-based supercapacitor nanomaterials. *Nanomaterials*, 7(2), 41.
- Wang, J., Dong, S., Ding, B., Wang, Y., Hao, X., Dou, H., . . . Zhang, X. (2016). Pseudocapacitive materials for electrochemical capacitors: from rational synthesis to capacitance optimization. *National Science Review*, 4(1), 71-90. doi:10.1093/nsr/nww072
- Winata, A. S., Devianto, H., & Susanti, R. F. (2021). Synthesis of activated carbon from salacca peel with hydrothermal carbonization for supercapacitor application. *Materials today: proceedings*, 44, 3268-3272.
- Yang, M., & Zhou, Z. (2017). Recent breakthroughs in supercapacitors boosted by nitrogen-rich porous carbon materials. *Advanced science*, 4(8), 1600408.
- Yuan, Y., Kong, Q., Zheng, Y., Zheng, H., Liu, Y., Cheng, Y., . . . Li, Y. (2022). Co-application of biochar and pyroligneous acid improved peanut production and nutritional quality in a coastal soil. *Environmental Technology & Innovation*, 28, 102886.
- Zhai, M., Shi, G., Wang, Y., Mao, G., Wang, D., & Wang, Z. (2015). Chemical compositions and biological activities of pyroligneous acids from walnut shell. *BioResources*, 10(1), 1715-1729.
- Zhang, W., Huo, X., Li, X., Park, S., Lin, L., Park, S. Y., . . . Piao, Y. (2022). Nitrogen and sulfur codoped porous carbon directly derived from potassium citrate and thiourea for high-performance supercapacitors. *Langmuir*, 38(33), 10331-10337.
- Zhao, J., & Burke, A. F. (2021). Review on supercapacitors: Technologies and performance evaluation. *Journal of Energy Chemistry*, 59, 276-291. doi:<https://doi.org/10.1016/j.ijechem.2020.11.013>

The background of the page features a large, faint, circular watermark of the Thammasat University seal. The seal is centered and contains the university's name in Thai script at the top and "THAMMASAT UNIVERSITY" in English at the bottom. In the center of the seal is a stylized emblem featuring a crown-like structure with horizontal lines and radiating elements.

APPENDICES

APPENDIX A

CHARACTERIZATION

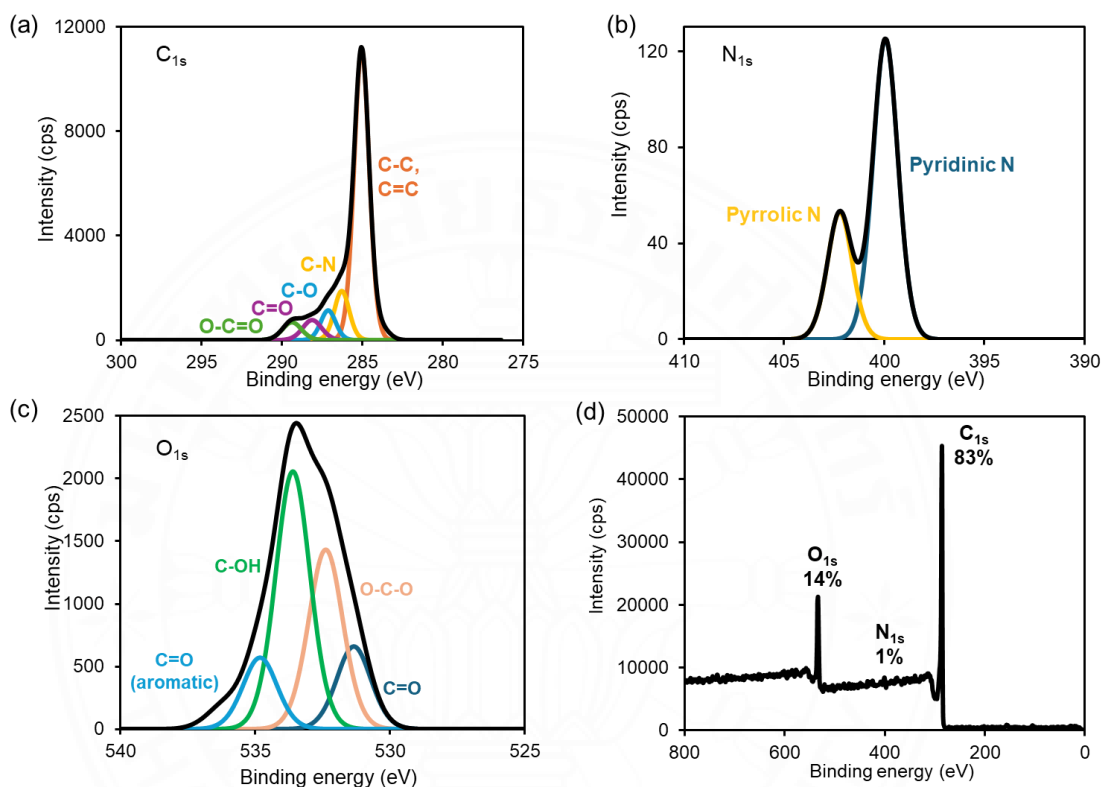


Figure 1A (a) high-resolution spectra of C_{1s} , (b) high-resolution spectra of N_{1s} , (c) high-resolution spectra of O_{1s} , and (d) Survey XPS spectra of AC700-1

APPENDIX B

ELECTROCHEMICAL MEASUREMENTS

Table 1B

Specific capacitance of AC different type electrode in 3M KOH electrolyte

Sample	AC800-1	AC800-2	AC800-3	AC700-1	AC700-2	AC700-3
Specific capacitance (F g ⁻¹)	175	157	164	450	510	475

Table 2B

Specific capacitance of AC700 in 3M KOH electrolyte in different scan rate

Scan rate (mV s ⁻¹)	Specific capacitance (F g ⁻¹)		
	AC700-1	AC700-2	AC700-3
5	543	640	564
10	527	586	551
30	450	510	475
50	386	476	416
70	330	448	367
100	276	411	306

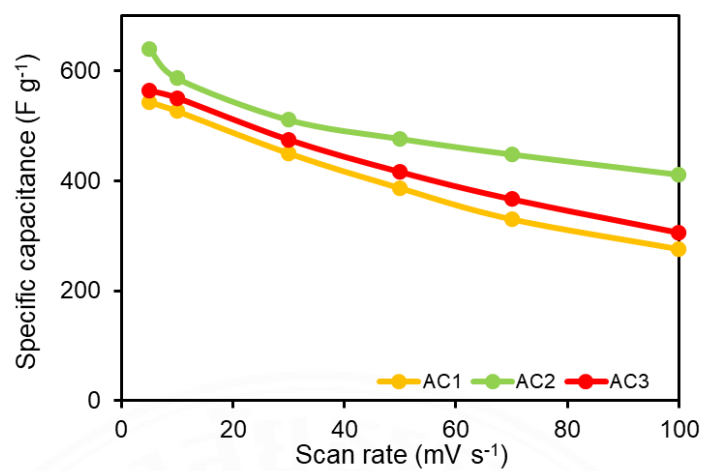


Figure 1B Relative between specific capacitance and scan rate of AC700 electrode and 3M KOH electrolyte

Table 3B

Specific capacitance of AC700 in 3M KOH/PA electrolyte in different scan rate

Scan rate (mV s ⁻¹)	Specific capacitance (F g ⁻¹)		
	AC700-1	AC700-2	AC700-3
5	515	880	782
10	493	806	701
30	434	672	569
50	391	560	497
70	353	497	398
100	309	425	345

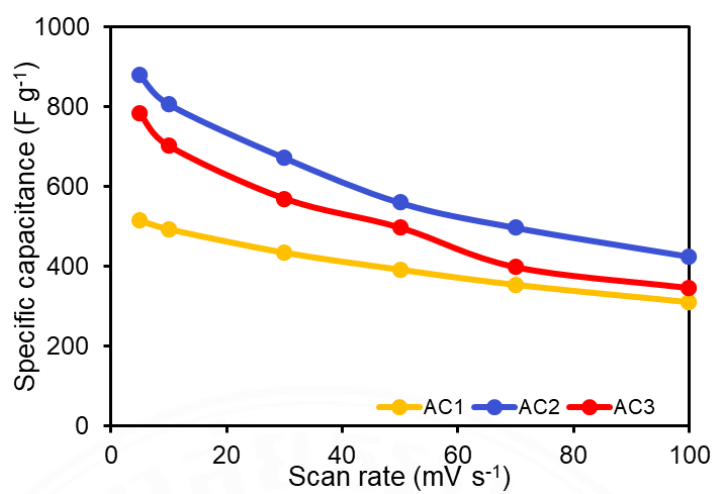


Figure 2B Relative between specific capacitance and scan rate of AC700 electrode and 3M KOH/PA electrolyte

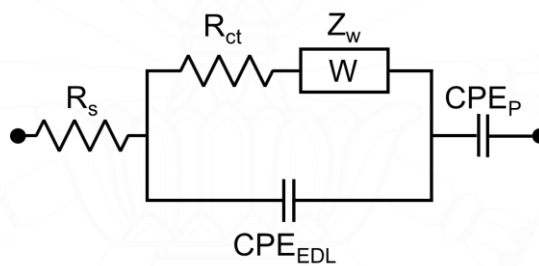


Figure 3B Equivalent circuit of supercapacitor

BIOGRAPHY

Name	Pattaramon Meefang
Educational Attainment	Academic Year 2021: Bachelor of Science (Chemistry), Thammasat University, Thailand

Publications

Pattaramon Meefang, Thanapat Jorn-am, Preeyanuch Supchocksoonthorn, and Peerasak Paoprasert. Activated carbon derived from hemp core biowaste with a doped heteroatoms and large specific surface area for supercapacitor applications. Pure and Applied Chemistry International Conference Proceedings, 2024, 401-405.

Activities and Awards	2024: Poster presentation at Pure and Applied Chemistry International Conference (PACCON 2024) 2023: Poster presentation at Pure and Applied Chemistry International Conference (PACCON 2023) 2022: Best Senior Project Award from Department of Chemistry, Faculty of Science and Technology, Thammasat University
-----------------------	---

Work Experiences	2024: Internship, International Affairs, Faculty of Science and Technology, Thammasat University 2023-2024: Teacher Assistant of Fundamental Chemistry Laboratory and General Organic Chemistry Laboratory at Faculty of Science and Technology, Thammasat University
------------------	--

2020: Internship, Center for Advanced
Scientific Instrumentation for Research,
Thammasat University

